J. Fluid Mech. (2018), *vol.* 857, *pp.* 748–783.
doi:10.1017/jfm.2018.783

Experimental investigation of turbulent suspensions of spherical particles in a square duct

Sagar Zade[1], Pedro Costa[1], Walter Fornari[1], Fredrik Lundell[1] and Luca Brandt[1,†]

[1]Linné Flow Centre and SeRC (Swedish e-Science Research Centre), KTH Mechanics, SE 100 44 Stockholm, Sweden

(Received 27 March 2018; revised 20 September 2018; accepted 20 September 2018)

We report experimental observations of turbulent flow with spherical particles in a square duct. Three particle sizes, namely $2H/d_p = 40$, 16 and 9 ($2H$ being the duct full height and d_p being the particle diameter), are investigated. The particles are nearly neutrally buoyant with a density ratio of 1.0035 and 1.01 with respect to the suspending fluid. Refractive index matched–particle image velocimetry (RIM–PIV) is used for fluid velocity measurement even at the highest particle volume fraction (20 %) and particle tracking velocimetry (PTV) for the particle velocity statistics for the flows seeded with particles of the two largest sizes, whereas only pressure measurements are reported for the smallest particles. Settling effects are seen at the lowest bulk Reynolds number $Re_{2H} \approx 10\,000$, whereas, at the highest $Re_{2H} \approx 27\,000$, particles are in almost full suspension. The friction factor of the suspensions is found to be significantly larger than that of single-phase duct flow at the lower Re_{2H} investigated; however, the difference decreases when increasing the flow rate and the total drag approaches the values of the single-phase flow at the higher Reynolds number considered, $Re_{2H} = 27\,000$. The pressure drop is found to decrease with the particle diameter for volume fractions lower than $\phi = 10\,\%$ for nearly all Re_{2H} investigated. However, at the highest volume fraction $\phi = 20\,\%$, we report a peculiar non-monotonic behaviour: the pressure drop first decreases and then increases with increasing particle size. The decrease of the turbulent drag with particle size at the lowest volume fractions is related to an attenuation of the turbulence. The drag increase for the two largest particle sizes at $\phi = 20\,\%$, however, occurs despite this large reduction of the turbulent stresses, and it is therefore due to significant particle-induced stresses. At the lowest Reynolds number, the particles reside mostly in the bottom half of the duct, where the mean velocity significantly decreases; the flow is similar to that in a moving porous bed near the bottom wall and to turbulent duct flow with low particle concentration near the top wall.

Key words: multiphase flow, particle/fluid flow, suspensions

† Email address for correspondence: luca@mech.kth.se

1. Introduction

The study of the flow of suspensions is a highly challenging endeavour. However, its sheer prevalence in natural flows and process industries has drawn the attention of researchers for a long time. Einstein (1906, 1911) first derived a formula for the effective viscosity of a suspension of spheres under dilute concentration. He was followed by many well-known scientists who contributed in different measure to unravel the mysteries of particle-laden flows. However, as ubiquitous as suspensions are, equally varied is their diversity in terms of particle size, density, concentration, shape, stiffness, etc. The analysis of suspensions is further complicated by the chaotic nature and multiscale dynamics of turbulent flows.

In the industrial use of technology, studies of particle-laden flows are relevant in areas such as transport of crushed coal, slurries, use of particle dispersions in paper coating and paints, foodstuffs, etc. In nature, flows include transport of sediments on and above the riverbed, red blood cells immersed in plasma, etc. All this justifies the need to gain a fundamental understanding of the physical phenomena occurring in suspensions.

1.1. *Flow in a square duct*

This article focuses on the interaction of rigid spherical particles with a fully developed turbulent flow in a square duct. A square duct poses interesting differences as compared to a plane channel flow, the turbulence in which is more often studied. In a square duct, the flow is inhomogeneous in the two cross-stream directions, whereas a plane channel as well as a round pipe has only one direction of inhomogeneity. However, compared to other duct geometries (e.g. a rectangular duct), these two inhomogeneous directions are symmetric. This inhomogeneity and wall-boundedness gives rise to a net cross-stream secondary flow of Prandtl's second kind (Prandtl 1926), which is superimposed on the primary axial flow. To note, secondary motion of Prandtl's first kind is much higher in magnitude (generally 10 %–40 % of the bulk velocity). This is driven by pressure gradients and is encountered in curved passages, where centrifugal forces act at an angle to the streamwise direction. On the other hand, the secondary flow of Prandtl's second kind is driven by gradients in the turbulence stresses, and its magnitude is smaller than the root-mean-square (r.m.s.) velocity of turbulent fluctuations and generally between 1 and 4 % of the bulk velocity in most straight ducts with non-circular cross-section. Nevertheless, these secondary motions, in the form of four pairs of counter-rotating vortices located at the duct corners (see figure 1 for a schematic), act to transfer fluid momentum from the centre of the duct to its corners, thereby causing a bulging of the streamwise mean velocity contours towards the corners. Also, their effect on the distribution of wall shear stress and heat transfer rates are quite significant (Demuren 1991). Therefore, the simple geometry of a square duct provides an excellent case to test and develop turbulence models that explore secondary flows of the second kind.

Probably, the first qualitative data on turbulence-driven secondary motion in non-circular ducts was presented by Nikuradse (1930) using flow visualization techniques. Brundrett & Baines (1964) found that the Reynolds normal-stress gradients were responsible for the generation of streamwise vorticity, manifesting in the form of secondary flow. Gessner (1973) showed that the secondary flow was due to the gradient of the Reynolds shear stress normal to the corner bisector. Later on, Gavrilakis (1992), Huser & Biringen (1993) and Uhlmann *et al.* (2007) investigated the mechanism behind the generation of secondary flow using numerical simulations.

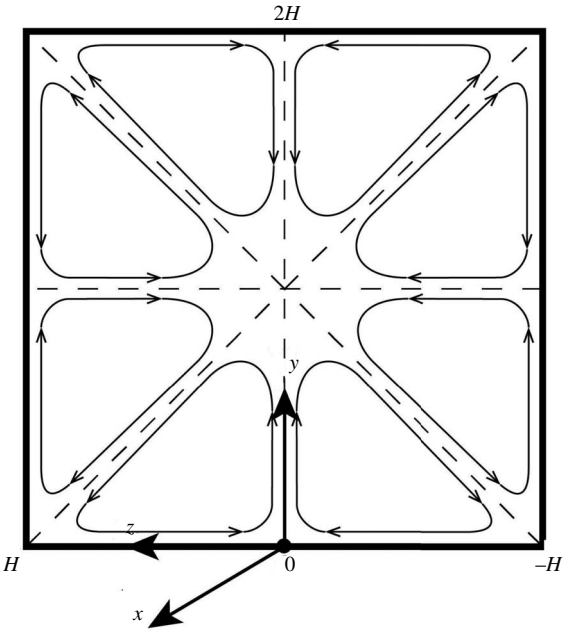

FIGURE 1. Schematic of secondary flow of Prandtl's second kind and coordinate system used in this study.

1.2. *Particle-laden flows*

The presence of the cross-stream secondary motion, explained in the above section, can have significant effects on the motion of a suspended particle phase. Even though there are limited studies on particle-laden turbulent flows in a square duct, phenomena observed in other canonical turbulent flow cases (e.g. channel or pipe flow) can help us in understanding the fundamental mechanisms of particle–fluid interactions.

1.2.1. *Numerical simulations using the point-particle assumption*

Starting with the relatively simpler assumption of point particles (where particle size is smaller than the Kolmogorov length scale of flow, η), various interesting phenomena have been observed in numerical simulations. In the one-way coupling regime (where the particle concentration is so small that it has negligible effect on the fluid phase), preferential concentration or clustering of particles within specific regions of the instantaneous turbulence field is observed (Eaton & Fessler 1994). In wall-bounded flows, particle inertia also induces a mean particle drift towards the walls, so-called turbophoresis (Reeks 1983), where the particles migrate from regions of high to low turbulence intensities. This migration is most pronounced when the particle inertial time scale nearly matches the turbulent near-wall characteristic time scale (Soldati & Marchioli 2009) and, close to the walls, particles tend to form streaky patterns (Sardina *et al.* 2012). In the two-way coupling regime (where the particle-to-fluid mass ratio is high enough to affect the fluid phase, but the volume ratio is still small so that inter-particle interactions and excluded-volume effects are negligible), Squires & Eaton (1990) and Elghobashi & Truesdell (1993) observed that particles alter the spectral distribution of the fluid turbulent kinetic energy in isotropic homogeneous flows. In wall-bounded flows, Kulick, Fessler & Eaton (1994) showed

that particles reduce the turbulent near-wall fluctuations, and Zhao, Andersson & Gillissen (2010) showed that this phenomenon can lead to drag reduction. In the case of a square duct, small inertial particles may preferentially migrate to the wall centre or to the corner regions (Winkler, Rani & Vanka 2004; Sharma & Phares 2006; Yao, Fairweather & Zhao 2014; Noorani *et al.* 2016).

1.2.2. *Simulations of finite-size particles and experiments*

In industrial and environmental flows, the particles often have sizes comparable to or larger than the Kolmogorov length scale, along with varying shape and stiffness, and the point-particle approximation is, generally, not applicable. Amongst such finite-sized particles, the most commonly studied cases involve mono-dispersed, rigid, spherical, neutrally buoyant particles suspended in an incompressible Newtonian fluid (Picano, Breugem & Brandt 2015; Fornari *et al.* 2016*a*; Lashgari *et al.* 2016; Ardekani *et al.* 2017).

Dilute laminar flow of finite-size particles is known to exhibit an increase in the effective viscosity (Guazzelli & Morris 2011). Bagnold (1954) showed how inter-particle collisions increase the effective viscosity in the highly inertial regime. Such inertial effects at the particle scale can induce other rheological effects, such as shear-thickening (Picano *et al.* 2013) or normal-stress differences (Kulkarni & Morris 2008; Yeo & Maxey 2013). These macroscopic changes could be explained by changes in the particle micro-structure (Morris 2009), as also shown by the recent direct experimental measurement of the suspension micro-structure in Blanc *et al.* (2013). Among other dependences, Fornari *et al.* (2016*b*) showed how the effective viscosity depends, in the special case of microfluidic applications, on the system confinement.

The suspended phase alters the critical Reynolds number Re for the flow to transition from the laminar to the turbulent state (see experiments by Matas, Morris & Guazzelli (2003) in a pipe flow and numerical simulations by Loisel *et al.* (2013) in a channel flow). Lashgari *et al.* (2014) showed how the distribution of viscous, turbulent and particle stresses (Batchelor 1970) varies when changing the particle volume fraction and Re in a plane channel flow.

Revisiting preferential concentration, now in the case of finite-sized particles, migration is also observed in wall-bounded laminar flows. In the viscous Stokes regime, particles migrate from regions of high shear to low shear due to irreversible interactions, e.g. towards the centreline in a Poiseuille flow (Guazzelli & Morris 2011). With an increase in particle Re, inertial effects become important and particles tend to move away from the centreline and equilibrate at an intermediate position due to the repulsive forces from the wall; see the tubular pinch effect in Segré & Silberberg (1962) and refer to Ho & Leal (1974) for an explanation of its mechanism. The final equilibrium position is found to depend on the ratio of the particle to pipe diameter, the particle Re and the bulk Re (Matas, Morris & Guazzelli 2004*b*). Particles also tend to form long trains in the flow (Matas *et al.* 2004*a*). Returning to the case of a square duct, Chun & Ladd (2006), in their lattice-Boltzmann simulations, observed the formation of particle trains that become unstable and break up into small clusters that tend to migrate towards the centre of the duct. However, in contrast to the formation of a continuous annular ring in a round pipe, particles in a square duct migrate to one of a small number of equilibrium positions: at the centre of the wall or near a corner (depending on Re). Choi, Seo & Lee (2011), Abbas *et al.* (2014) and Miura, Itano & Sugihara-Seki (2014) experimentally measured the migration of particles in laminar flow in a square duct at low volume fractions. Kazerooni *et al.*

(2017) studied numerically the laminar flow in a square duct at different Re, up to a particle volume fraction $\phi = 20\,\%$ and for different duct-to-particle size ratios. According to their study, particles largely move to the corners at lower volume fractions and at higher Re. Recently Fornari *et al.* (2018*a*) numerically investigated turbulent flows of a suspension of spherical rigid particles in a square duct up to a volume fraction of 20 % and found that, at the highest volume fraction, particles preferentially accumulate in the core region and the intensity of the secondary flows reduces below that of the unladen case.

Most of the above observations pertaining to higher volume fractions are made using numerical tools, due to the difficulties in tackling such problems experimentally. External bulk measurements such as the overall pressure drop in the presence of particles (mostly sedimenting slurries in pipe flows) have been reported in Doron, Granica & Barnea (1987) and Kaushal & Tomita (2002) amongst others. However, detailed velocity and concentration measurement in the interior of the suspension at high concentrations is rare, especially in turbulent flows. A few studies in this direction are highlighted below.

Hampton *et al.* (1997) made use of magnetic resonance imaging velocimetry (MRI-V) to study the evolution of the axial velocity and concentration distribution of neutrally buoyant particles in a Poiseuille flow up to a particle volume fraction of 50 %. These authors found that the entrance lengths for the development of the concentration and velocity fields rapidly decrease as volume fraction and particle-to-pipe ratio was increased. Han *et al.* (1999) extended MRI-V measurements to particles with non-negligible inertia ($Re_p \approx 0.2$) so that inertial migration towards regions between the pipe axis and the wall is competing with particle–particle interaction that pushes the particles towards the centre. The parabolic velocity profile becomes blunted due to migration of particles towards the centre. Another experimental technique used for suspensions is laser Doppler velocimetry (LDV). Koh, Hookham & Leal (1994) used LDV in a rectangular channel flow and also observed that the particle concentration distribution possessed a maximum near the channel centreline and a minimum at the channel walls (see also Lyon & Leal 1998). Frank *et al.* (2003) studied the particle migration in Brownian suspensions (colloidal particles) in Poiseuille flow using confocal microscopy, owing to its higher spatial resolution. Using PIV in a matched refractive index medium, Abbas *et al.* (2017) recently studied the laminar flow of concentrated non-colloidal particles ($\phi = 70\,\%$) and observed a Newtonian-like variation of pressure drop with bulk velocity even though the mean velocity profile clearly exhibited a shear-thinning behaviour. They used the notion of effective viscosity, based on the local particle concentration, in the framework of the suspension balance model (Zarraga, Hill & Leighton Jr 2000), to explain this peculiar behaviour. All the above experimental studies focused on low-Reynolds-number laminar flows. Recently, Gurung & Poelma (2016) used ultrasound imaging velocimetry (UIV) to show that usable data can be obtained even in turbulent particle-laden flows at moderately high volume fractions. However, it was not possible to differentiate between the statistics of the fluid and the particle phase. MRI-V, on the other hand, suffers from low spatial and temporal resolutions when studying complex suspensions in turbulence. Furthermore, they also involve heavy procedures and expensive tools that make them somewhat difficult to use.

1.2.3. *Refractive index matched–particle image velocimetry (RIM–PIV)*

The *de facto* workhorse in the field of experimental flow measurement is PIV, which is an optical measurement technique requiring the use of an optically transparent

solution as the working fluid. Measuring velocity in suspensions using PIV relies on the use of particles that are transparent, i.e. the refractive indices of the fluid and particles are nearly the same with respect to the wavelength of the light used for illumination. However, the particles usually available are composed of materials such as plastic, metal, glass etc. For these dispersed particles, a volume fraction of 0.5 % in a domain of 5–10 cm has been indicated as the limit (Poelma, Westerweel & Ooms 2006). There are, of course, some limited options available for refractive-index-matching (RIM) fluids to enable the use of PIV (see Wiederseiner *et al.* 2011), but they are often difficult to scale up due to issues related to the long-term properties of the suspending solution, thermal stability, handling and cost.

Therefore, there is a need for particles that display long-term optical transparency independent of moderate changes in temperature and solution properties, and that can be used in a fluid that is readily available and easy to handle (e.g. water). Super-absorbent hydrogel particles offer such an advantage. These particles have been successfully used to study the trajectories of large spheres (with size $\approx$100 times the Kolmogorov length scale η) in three dimensions in Klein *et al.* (2012), where the particle surface was meticulously grafted with fluorescent particles to track their complete motion. Bellani *et al.* (2012) studied the effect of Taylor-microscale-sized particles on homogeneous isotropic turbulence. In order to track particle rotation, small PIV tracer particles were embedded inside the macroparticle, made via injection moulding. However, the particle volume concentration (ϕ) used in their experiments was only 0.14 %. The simultaneous fluid–particle PIV method requires a large number of tracers that are all internal to a single macroparticle with unambiguous borders, which may be an issue for small macroparticles and large concentrations (Byron & Variano 2013).

Finite-size particle modulations of the flow cannot be captured by simple modelling techniques such as those using an effective viscosity or other more complex constitutive laws for the stresses, as shown, for example, in turbulent channel flows in Costa *et al.* (2018). Even for laminar flows, finite-size particle effects, e.g. particle migration, result in large deviations of flow characteristics from the predictions based on an effective fluid model and exhibit a complex dependence on volume fraction and Reynolds number, as shown in a recent study for a laminar square duct by Manoorkar *et al.* (2018). Therefore, in this study, we perform detailed experiments in a square duct, for a range of bulk Reynolds number (Re_{2H}), particle concentration (ϕ) and particle size ratio ($2H/d_p$), so as to relate the bulk observables to the local microscale dynamics.

1.3. *Outline*

The structure of this article is as follows. First, we describe the experimental facility and details about the data acquisition. The following results section includes validation studies with a single-phase Newtonian fluid, pressure drop measurements and velocity profiles for different flow cases with particles. Finally, we discuss the observations with a focus on the highest (full suspension regime) and the lowest (sedimentation regime) Reynolds number, also referring to the numerical simulations in Fornari *et al.* (2018*a*) for neutrally buoyant particles.

2. Experimental set-up

2.1. *Particles*

The particles are commercially procured super-absorbent (polyacrylamide-based) hydrogel. They are delivered with a range in diameter from 0.5 mm to 1.1 mm (see

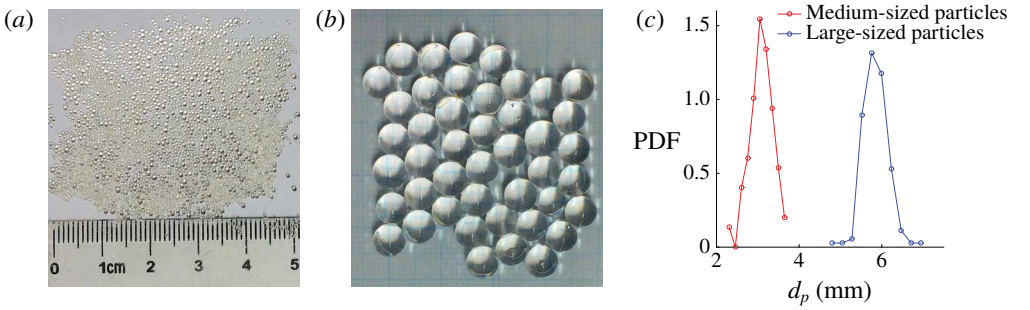

FIGURE 2. (Colour online) Image of the particles (*a*) before expansion (all sizes, in dry state), (*b*) after expansion (only large-sized particles) and (*c*) size distribution of medium and large-sized particles (see table 1 for details about particle nomenclature).

figure 2*a*). Once mixed with tap water and left submerged for approximately 1 day, they grow to an equilibrium size between 3 and 6 mm. Particles are graded into different sizes using a range of sieves, prior to expansion in water (as they become softer and would break while sieving after expansion), into two batches: 0.55 ± 0.05 mm and 1.0 ± 0.05 mm, which expanded to a size of 3.05 ± 0.8 mm (three times standard deviation) and 5.60 ± 0.9 mm (see figure 2*b*). The particle size was determined by a digital imaging system and from the PIV images of particles in flow. Figure 2(*c*) shows the probability distribution function (PDF) of the particle size for the medium- and large-sized particles. The fact that a Gaussian-like particle size distribution, with small size variance, has a small effect on the flow statistics has been shown in Fornari, Picano & Brandt (2018*b*). Hereafter, the 3.05 mm particles ($2H/d_p \approx 16$) will be denoted as 'medium-sized particles' or 'MP', whereas the 5.60 mm particles ($2H/d_p \approx 9$) will be denoted as 'large-sized particles' or 'LP'.

We also use smaller particles, denoted 'small-sized particles' or 'SP', which are 1.25 mm in diameter ($2H/d_p \approx 40$). These were also procured commercially. The SP have slightly different density and optical properties as compared to the larger ones. In this case, a small quantity of tracer particles (approximately 4 % w w^{-1} in the dry state) was added during their manufacturing process to facilitate the tracking of particle rotation (see Bellani *et al.* 2012). At the particle concentrations used in this study, it was difficult to visualize the fluid flow beyond a few particle diameters due to the attenuation of light in such a turbid medium. Under such conditions, it was hard to differentiate the border of the particle from the fluid. Thus, PIV was not possible with SP and only pressure drop measurements are reported. On the other hand, the MP and LP, without tracers inside, were relatively transparent, so as to enable visualization up to a bulk volume fraction of 20 %. (Note that, at a bulk volume fraction of 20 %, there are areas where the local volume fraction exceeds more than twice this nominal value due to settling or flow-induced migration.) To enhance the contrast of the MP and LP, a small amount of Rhodamine was added to the water in which the particles expand. Due to the absence of tracers inside MP and LP, we could only measure translational motion.

The density of the particles was determined using two methods: (i) by measuring the volume displacement by a known mass of particles and (ii) by determining the terminal settling velocity in a long liquid settling column. In the first method, a known mass of fully expanded particles was put in a water-filled container of uniform diameter. The rise in the level of water due to the particles was measured using a

$2H/d_p(\approx)$	$\frac{\rho_p}{\rho_f}$	Name	Appearance	Measurements performed
40	1.01 ± 0.003	Small particles (SP)	'Milky'	Pressure drop only
16	1.0035 ± 0.0003	Medium particles (MP)	'Clear'	Pressure drop and velocity
9	1.0035 ± 0.0003	Large particles (LP)	'Clear'	Pressure drop and velocity

TABLE 1. Particle properties and the type of measurements performed.

very precise laser distance meter (optoNCDT 1710, Micro-Epsilon Messtechnik GmbH, resolution = 0.5 μm). In the second method, a single particle with a known diameter was gently dropped in a long vertical pipe, filled with water, wide enough so as to minimize the wall effects. The settling velocity is determined (after it has reached steady state) by noting the time to pass by regularly placed distance markers. The relation for drag force F on a settling particle in Crowe *et al.* (2011),

$$\frac{F}{\rho_f U_T^2 A} = \frac{12}{Re_p}(1 + 0.15Re_p^{0.687}), \tag{2.1}$$

applicable in the transitional regime $1 < Re < 750$, was used to relate the particle diameter d_p and terminal velocity U_T to the unknown particle density ρ_p. A is the projected area of the particle. In the above, Re_p is the particle Reynolds number given by $\rho_p U_T d_p/\mu_f$, where μ_f is the dynamic viscosity of the liquid. Both the above tests were performed at a room temperature of approximately 20 °C and yielded nearly the same value of density. The latter method was preferred as it was less sensitive to measurement uncertainties. Table 1 lists the properties of the particles used in the experiments.

Our solid-gel-like particles are elastically deformable, but the forces (shear and pressure) applied by the fluid were not sufficient to deform them. This was ascertained by observing the particle shape in the PIV movies. Therefore, these particles can, for the purpose of this study, be considered as rigid.

Since the gels consist mostly of fluid, there exists a layer of fluid between the gel and the contacting surface, making them slippery, so they are able to slide with friction coefficients that may be smaller than those observed in solid materials. Also in contrast to hard solid–solid contact, the coefficient of sliding friction has been observed to decrease with increasing normal force (Gong *et al.* 1997) and increase with sliding velocity along with being a function of contact area for the gels. But, for our spherical particles, in the limit of negligible deformation, we can assume a single point of contact between two spheres or a sphere and the wall. A recent study (Cuccia 2017) has measured the friction coefficient between a sphere and flat surface, both made from a polyacrylamide-based gel (which is the same material that our particles are made up of). They observed values of approximately 10^{-2} at sliding velocities between 0.001 and 0.1 m s^{-1}.

2.2. *Experimental rig*

The experiments were performed in a square duct that is 50 mm × 50 mm in cross-section and 5 m in length. The entire duct is made of transparent Plexiglas, permitting visualization throughout its length. Figure 3(*a*) shows a schematic of the flow loop. The fluid is recirculated through a conical tank, open to the atmosphere, where the

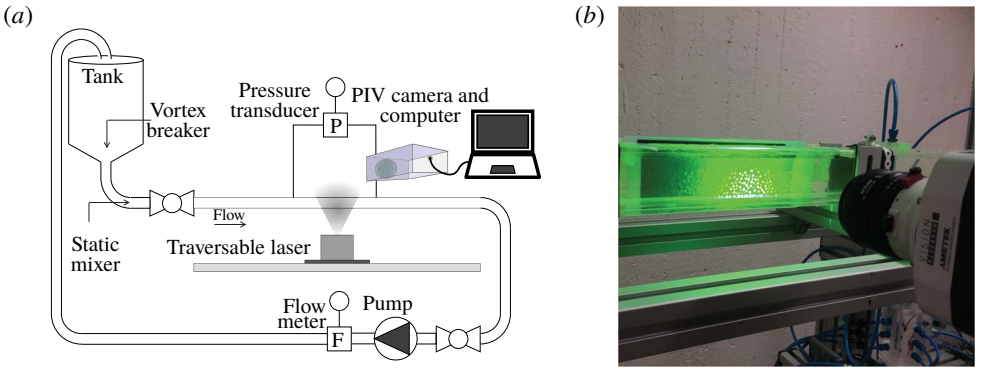

FIGURE 3. (Colour online) (*a*) Schematic of the flow loop. (*b*) Photo of the section where PIV is performed.

particle–fluid mixture can be introduced. A vortex breaker has been installed at the conical end of the tank to prevent entrainment of air due to suction at higher flow rates. A static mixer is mounted close to the inlet of the duct with the intention of neutralizing any swirling motions that may arise from the gradual 90° bend at the exit of the tank. It is followed by a section providing a smooth transition from a circular to a square cross-section. Finally, to trigger turbulence at the inlet, a friction tape is lined on the inner walls of the Plexiglas duct at its entrance. The temperature of the solution is maintained at nearly 20 °C by means of an external heat exchanger in the tank. Flexible corrugated piping is used to minimize the induction of vibrations from the pump to the duct. As explained in § 2.1, the particles are soft and can break under high stresses. In order to minimize mechanical breakage of the particles, a very gentle disc pump (Discflo Corporations, CA, USA) has been chosen. It can pump rather large particles at reasonably high volume concentration without pulsations. Such a pump has been previously used to study the laminar–turbulent transition in flow of polymer solution, where the degradation of the polymer chains should be minimized to achieve high drag reduction for longer time (Draad, Kuiken & Nieuwstadt 1998).

It was observed that the particles marginally shrink in size, while retaining their spherical shape, over many flow cycles. This may be due to the mechanical degradation of the particles reducing the water retention capability of the polymer matrix. To minimize the influence of such long-term deviations in size and density, the time of experiments was kept short enough to have reasonably constant properties of the particles during the course of the data acquisition, but long enough to get statistically stationary results. The maximum measurement time for any given case did not exceed 20 min.

2.3. *Volume flow and pressure measurements*

An electromagnetic flowmeter (Krohne Optiflux 1000 with IFC 300 signal converter, Krohne Messtechnik GmbH, Germany) is used to measure the flow rate. Since the conductivity properties of the hydrogel particles are similar to those of water, the flow rate measured by the electromagnetic flowmeter is equal to the flow rate of the mixture. To reduce the risk of faulty readings caused by electrical disturbances in the flowmeter, another flowmeter with a ceramic electrode was also tested. The results compared at different particle concentrations and flow rates indicated a deviation less

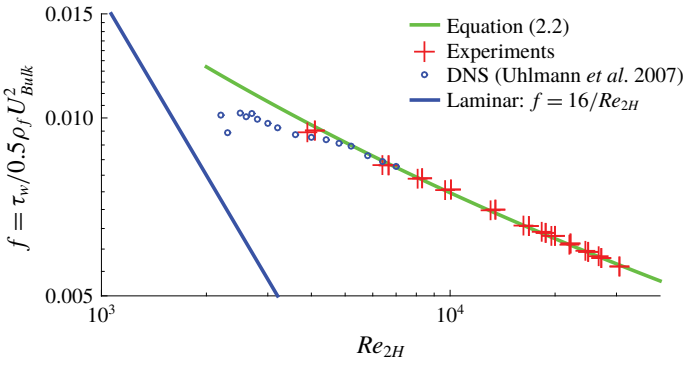

FIGURE 4. (Colour online) Comparison between experiments, DNS simulations and empirical correlation for the Fanning friction factor f as a function of bulk Reynolds number Re_{2H} for single-phase Newtonian fluid.

than 1 %. The Reynolds number Re_{2H}, used hereafter, is based on the flow rate of the mixture of solid and liquid phase, the viscosity of the liquid and full height of the duct $2H$.

The pressure drop is measured across a length of $54H$ in a region of the duct that is nearly $140H$ from the inlet (the turbulent flow was seen to be fully developed at this entry length) using a differential pressure transducer (0–1 kPa, model: FKC11, Fuji Electric France, S.A.S.). At a given streamwise location, two pressure tappings (one at the top wall and other at the bottom wall) were precisely drilled in the wall-normal direction at the centre plane of the duct. The pressure tubes emerging from these two upstream holes were joined together into one single tube, then connected to the high-pressure side of the pressure transducer. A similar connection was made at the downstream position of the duct to the low-pressure side of the pressure transducer. Additional pressure tappings were also made to study the evolution of pressure drop over the streamwise length. Figure 4 shows reasonable agreement between the friction factor $f = \tau_w/(\rho_f U_{Bulk}^2/2)$ (U_{Bulk} is the bulk velocity given by the ratio of the flow rate to the cross-sectional area) for the single-phase flow measured in our square duct and the empirical correlation given in Duan, Yovanovich & Muzychka (2012),

$$f = \left(3.6 \log_{10}\left(\frac{6.115}{Re_{\sqrt{A}}}\right)\right)^{-2}. \tag{2.2}$$

The Reynolds number $Re_{\sqrt{A}}$ is based on the characteristic length given by the square root of the cross-section area A. The friction velocity is given by $u_\tau = \sqrt{\tau_w/\rho_f}$. Data acquisition from the camera, flowmeter and pressure transducer is performed using a NI-6215 DAQ card using LabVIEW™ software.

2.4. *Velocity measurement technique*

The coordinate system used in this study is indicated in figure 1. The velocity field is measured using 2D particle image velocimetry (2D-PIV) in three cross-stream planes: $z/H = 0$, 0.4 and 0.8, where H is the half-width of the duct. These measurements are performed at a streamwise distance of $x/H \approx 150$ from the entrance of the duct. A traversable continuous wave laser (wavelength = 532 nm, power = 2 W) and

a high-speed camera (Phantom Miro 120, Vision Research, NJ, USA) are used to capture successive image pairs. Figure 3(*b*) shows the PIV set-up. The laser light travels from the bottom to the top of the duct.

For imaging the full height of the duct, a resolution of approximately 60 mm 1024 pixels^{-1} was chosen. The frame rate (acquisition frequency) was chosen so that the maximum pixel displacement did not exceed a quarter of the size of the final interrogation window (IW) (Raffel *et al.* 2013). Images were processed using an in-house, three-step, FFT-based, cross-correlation algorithm (used in Kawata & Obi 2014). The first step consisted of basic PIV with a large IW size (48 pixel × 48 pixel), followed by the discrete-window-shift PIV at the same IW size and, finally, the central-difference-image-correction method (Wereley & Gui 2003) with the final IW size (32 pixel × 32 pixel). The degree of overlap can be estimated from the fact that the final resolution is 1 mm × 1 mm. Usually 1000 image pairs have been observed to be sufficient to ensure statistically converged results.

Figure 5(*a–c*) shows the streamwise velocity of single-phase Newtonian flow measured at three different sections: $z/H = 0$, 0.3 and 0.6, compared with previously published DNS simulations at $Re_{2H} = 5800$ (Uhlmann *et al.* 2007). The experimental Reynolds number is slightly lower at $Re_{2H} \approx 5540$. The corresponding Reynolds stresses are reported in figure 5(*d–f*) to confirm that the mean velocity and turbulence statistics are in good agreement with the simulations. The resolution is approximately 1 mm × 1 mm in figure 5(*a–f*), where the measurements cover the full height of the duct. This resolution is suitable for velocity statistics in the bulk of the flow, away from the walls, but it is inadequate in the near-wall region, characterized by a large variation in velocity over a very small distance. Therefore, a separate measurement is conducted by zooming the camera on a small region close to the wall with a resolution of approximately 0.35 mm × 0.35 mm. Figure 5(*g–i*) displays the streamwise velocity profile (in wall units) close to the wall. These measurements close to the wall show even better agreement with the simulations for the location and magnitude of the peak in the variance of the velocity fluctuations (not shown).

The experiments with particles are performed at a higher Re_{2H}, ranging from 10 000 to 27 000. At these high Re_{2H}, the magnitude of the secondary flow was observed to be less than 2 % of the bulk velocity in the three spanwise planes where the velocities were measured. The measured wall-normal velocity profiles were extremely sensitive to the PIV arrangement (parallelism of the camera, concentration of PIV tracers, etc.) and exhibited variation (related, for example, to point of zero-crossing, top-down symmetry) between similar experiments. Hence, to prevent observations beyond our measurement capabilities, we do not report the secondary flow velocity. However, the effect of such secondary motions on the streamwise velocity distribution are of a relatively larger magnitude; hence, such effects are properly captured by the PIV.

Figure 6 depicts one image from a typical PIV sequence for particle-laden flow. As mentioned earlier, the contrast between particle and fluid was enhanced by using a small quantity of Rhodamine. Raw images captured during the experiment were saved in groups of two different intensity levels. The first group of images (an example being figure 6*a*) was used for regular PIV processing according to the algorithm mentioned in § 2.4. The second group of images (cf. figure 6*b*) was used for detecting the particles only. The images were sharpened and their intensity adjusted so that particles could be easily detected using a circular Hough transform (Yuen *et al.* 1990). From the detected particles in image A and B of the PIV sequence, a nearest-neighbour approach was used to determine their translational motion. Particles that were detected only in one image of the pair were, thus, eliminated by the PTV

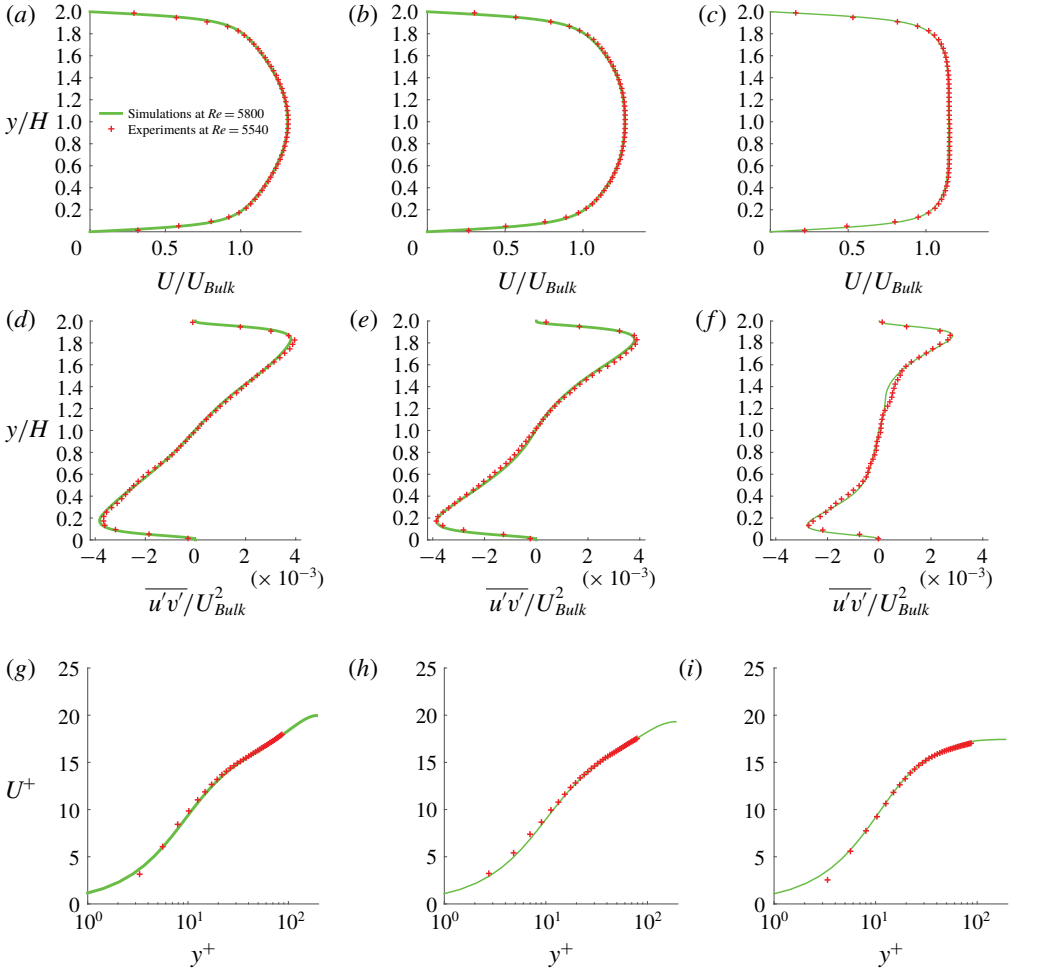

FIGURE 5. (Colour online) Comparison of experimental mean-streamwise velocity profiles with DNS of single-phase flow at three spanwise planes: (*a*) $z/H = 0$, (*b*) $z/H = 0.3$ and (*c*) $z/H = 0.6$. (*d–f*) Corresponding Reynolds stress and (*g–i*) mean-streamwise velocity in wall units. The Reynolds number Re_{2H} for DNS and experiments is 5800 and 5540, respectively.

algorithm. For the Eulerian PIV velocity field, we define a mask, which assumes the value 1 if the point lies inside the particle and 0 if it lies outside. The fluid phase velocity is thus determined on a fixed mesh. The particle velocity is determined using PTV at its centre, which is assigned to the grid points inside the particle (mask equal to 1). The velocity field of the particle phase is now available at the same grid points as that of the fluid, and the ensemble averaging, reported later, is phase-averaged statistics. Figure 6(*c*) shows the combined fluid (PIV) and particle (PTV) velocity field.

As will be shown later in the results section, the area concentration ϕ_{Area} in some regions of the flow was as high as 50 %. At such a high concentration, the inter-particle distance is small and particles could not be detected at all times. In addition, the detection was slightly inefficient close to the top wall at the highest concentration considered because the intensity of the laser light reduces.

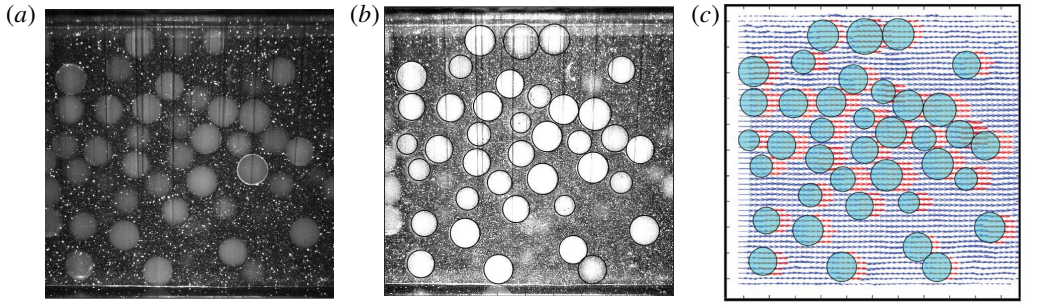

FIGURE 6. (Colour online) (*a*) Image for PIV analysis, (*b*) image for particle detection and PTV analysis and (*c*) combined fluid PIV and particle PTV velocity vectors for $\phi = 20\,\%$ of LP at $Re_{2H} \approx 27\,000$.

Also, particles on the bottom wall cast shadows on the particles above them, making them appear as bright circles cut by dark lines. Detecting such faint 'striped' circles was an issue for the particle detection algorithm. These are the reasons why we decided to limit the particle bulk concentration to $\phi = 20\,\%$ in our study.

3. Results

We measure the pressure drop at three particle volume fractions ($\phi = 5$, 10 and 20 %), three particle sizes ($2H/d_p \approx 40$, 16 and 9) at four different Reynolds numbers ($Re_{2H} \approx 10\,000$, 15 000, 20 000 and 27 000). Particle and fluid velocity fields have been measured for all particle sizes except for the smallest particles, i.e. $2H/d_p \approx 40$, as they were not transparent enough (see previous section).

Even though the particle-to-fluid density ratio is very close to 1 (see table 1), sedimentation effects are visible, especially at low Re_{2H}. To illustrate this, figure 7 shows a typical PIV image at $\phi = 5\,\%$ for MP and LP at the lowest and highest Re_{2H}. For the lowest Re_{2H}, most of the particles occupy the lower half of the duct (see figure 7*a,b*). As Re_{2H} is increased, more particles are drawn into suspension (see figure 7*c,d*).

To quantify the role of gravity, we consider two non-dimensional numbers: the Shields number Sh and the Rouse number Ro. The former, $Sh = \tau_w/(\rho_p - \rho_f)gd_p$, quantifies the relative strength of shear forces and gravitational forces. Here, τ_w is the wall shear stress and g is the acceleration due to gravity. A critical threshold value of Sh is generally used to determine the onset of particle motion on a bed (Shields 1936). Figure 8(*a*) depicts Sh for the different cases in our experiment, which are well above the critical value. With increasing Sh, more particles are suspended and the transport of sedimenting particles depends on the ratio of the particle sedimenting velocity U_T to the characteristic turbulent velocity u_τ, i.e. the Rouse number $Ro = U_T/\kappa u_\tau$ (Rouse 1937). Here κ is the von Kármán constant. In our experiments, Ro ranges from values for bed load (where particles are transported along the bed: large particles LP at lowest Re_{2H}) to full suspension (all particles are suspended by the fluid turbulence: small particles SP at highest Re_{2H}) as shown in figure 8(*b*). The different regimes of particle transport given in Fredsøe & Deigaard (1992) are indicated by the different background colours in figure 8(*b*).

To give an estimate of the difference in the time scales of the flow and particles, figure 8(*c*) depicts the particle Stokes number $St = (\rho_p {d_p}^2/18\rho_f \nu_f)/(H/U_{Bulk})$ based on

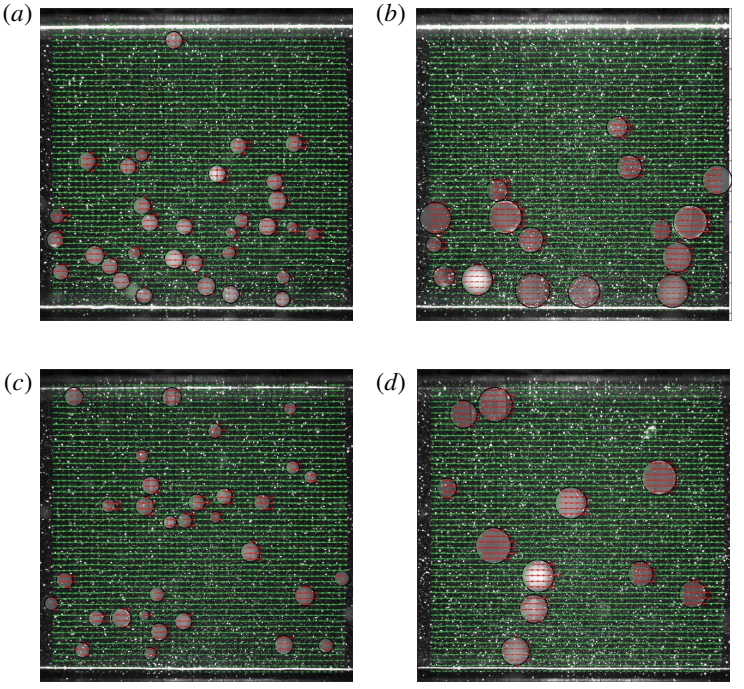

FIGURE 7. (Colour online) Effect of density difference on the particle distribution: non-negligible particle sedimentation in (*a*) $2H/d_p = 16$, $Re_{2H} \approx 10\,000$ and (*b*) $2H/d_p = 9$, $Re_{2H} \approx 10\,000$. Particles in nearly full suspension in (*c*) $2H/d_p = 16$, $Re_{2H} \approx 27\,000$ and (*d*) $2H/d_p = 9$, $Re_{2H} \approx 27\,000$. The volume fraction in all the above figures is $\phi = 5\,\%$.

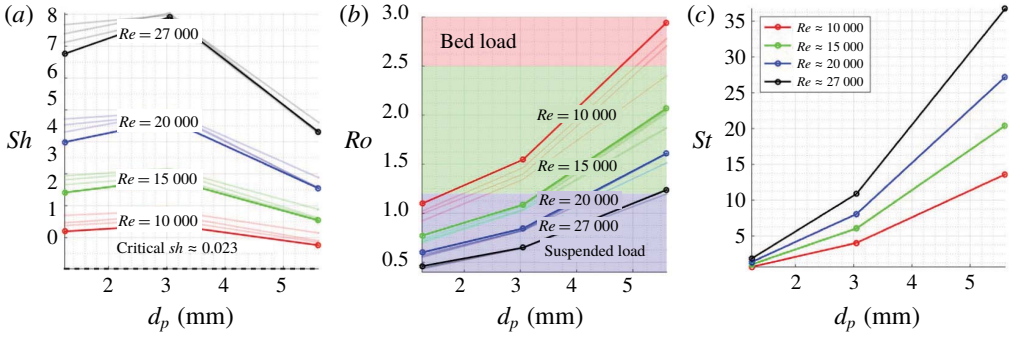

FIGURE 8. (Colour online) Particle Shields number *Sh* (*a*), Rouse number *Ro*, based on the friction velocity u_τ (*b*), and Stokes number *St* (*c*), as a function of particle size d_p and Reynolds number Re_{2H}. The solid lines in all figures use u_τ and τ_w from single-phase flow (i.e. $\phi = 0\,\%$) as scaling factors. The thin lines in figures (*a*) and (*b*) are obtained by dividing with the values pertaining to particle-laden flow at $\phi = 5$, 10 and 20 %.

the fluid bulk time scale. To estimate the particle size compared to the inner length scales of the flow, we note that the small particle (SP) diameter is approximately $15\delta_\nu$ (where $\delta_\nu = \nu/u_\tau$ is the viscous length scale) at the lowest $Re_{2H} \approx 10\,000$. So, the SP are already approximately three times larger than the thickness of the viscous sublayer. On the other limit, the size of LP is approximately $165\delta_\nu$ at the highest $Re_{2H} \approx 27\,000$.

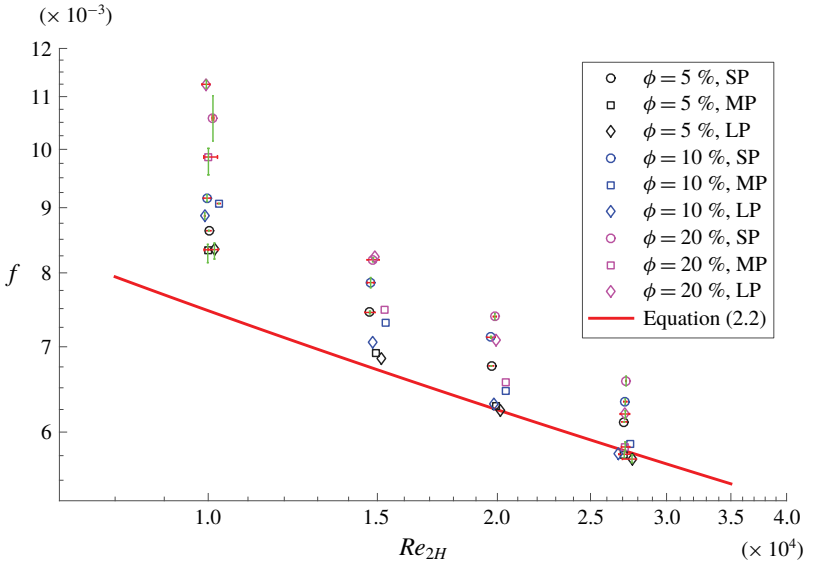

FIGURE 9. (Colour online) Friction factor f as a function of Reynolds number, Re_{2H}, particle size d_p and volume fraction ϕ. Symbols with the same colour denote the same concentration. Symbols with same shape denote the same particle size. The solid red line corresponds to single-phase flow.

3.1. *Pressure drop*

We first report the overall pressure drop, in terms of the friction factor f, as a function of the Reynolds number Re_{2H} for all the particle sizes d_p and volume fractions ϕ considered in this study. This is shown in figure 9. Error bars are reported for those experiments that were repeated and correspond to the maximum and minimum values observed for the specific case: their small values suggest that the uncertainty in the measurements is relatively small.

As seen in the figure, the drag increase due to the particles strongly reduces as Re_{2H} is increased. At the lowest $Re_{2H} \approx 10\,000$, the pressure drop increases in the presence of particles by 10 %–50 %, depending on the particle size and volume fraction. At the highest $Re_{2H} \approx 27\,000$, it varies only from -2 to 14 % of the single-phase value. These changes with Re_{2H} will be related to the particle inertia and to the change in the particle dynamics: from sedimenting to fully suspended particles as seen in figure 7. At the lowest $Re_{2H} \approx 10\,000$, particles constitute a moving bed of higher concentration at the bottom of the duct. At this low Re_{2H} the friction factor mainly depends on the particle volume concentration and increases with ϕ. The particle size has a minor role on the pressure drop at the lowest concentrations considered, i.e. at $\phi = 5$ and 10 %. At $\phi = 20$ %, conversely, LP cause the largest pressure drop and MP cause the lowest pressure drop. So, we observe a dependence on the particle size at $\phi = 20$ %.

As the Reynolds number is increased, most of the particles are now dispersed in suspension, and hence the pressure loss depends upon the mutual interaction between particles and turbulence in the bulk of the flow and close to the wall. An interesting observation is that at $Re_{2H} \approx 27\,000$, the different concentrations of MP lead to nearly the same pressure drop as the single-phase flow, which we will explain as a result of two counteracting effects.

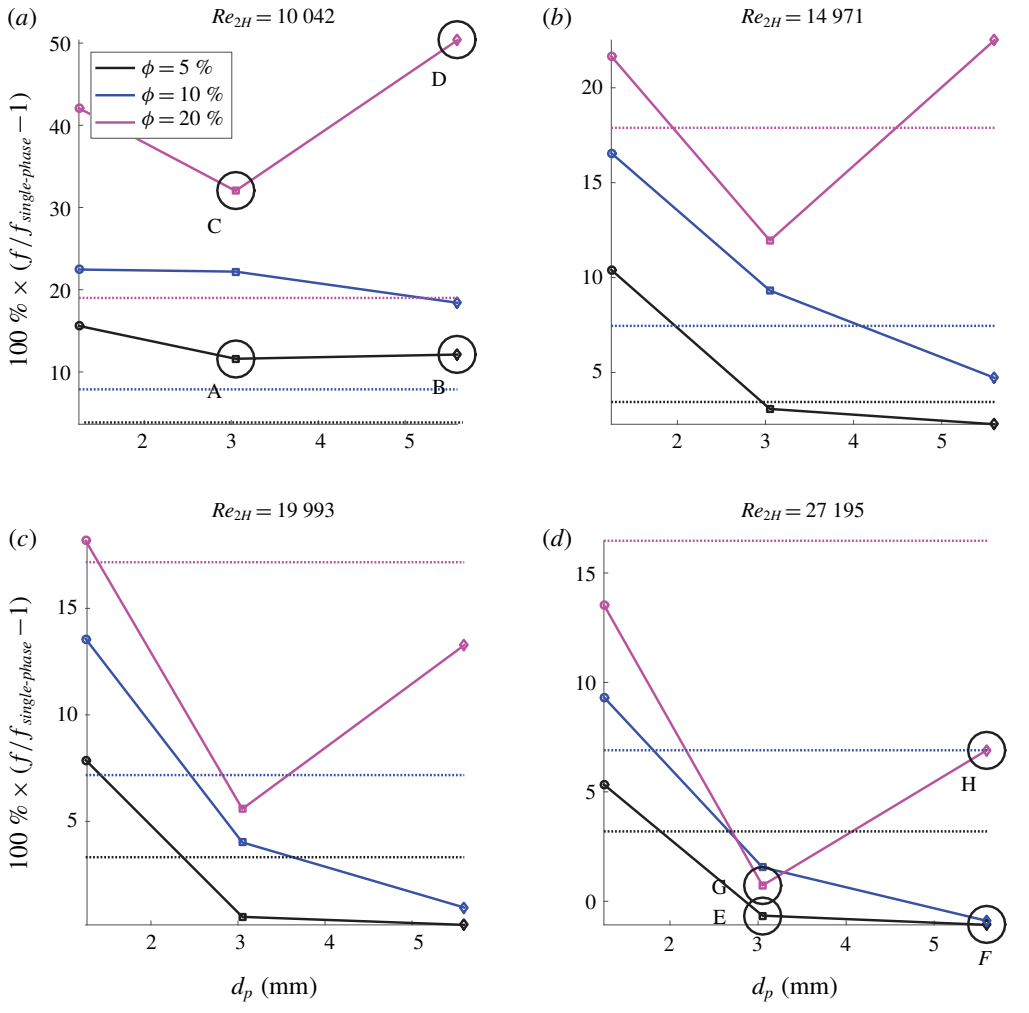

FIGURE 10. (Colour online) Percentage change of the friction factor f with respect to the friction factor of the single-phase flow versus the particle size d_p and volume fraction ϕ for four different Re_{2H} (indicated on the top of each subfigure). The dashed lines (same colour as for the data at the corresponding ϕ) indicate the friction factor obtained with the values of the effective suspension viscosity from the Eilers fit (3.1). The large circles in (*a*) and (*d*) correspond to the cases where PIV and PTV data are reported.

To better understand the changes in the friction factor at each Re_{2H}, the data points in figure 9 are displayed as relative change with respect to the single-phase flow in figure 10. The dashed lines show the friction factor based on an effective suspension viscosity, obtained from the Eilers fit (Stickel & Powell 2005); this empirical formula relates the effective viscosity to the nominal volume fraction ϕ in the limit of vanishing inertia,

$$\frac{\eta_e}{\eta} = \left(1 + \frac{5}{4}\frac{\phi}{1 - \phi/0.65}\right)^2. \tag{3.1}$$

The effective viscosity η_e is used to compute an effective Reynolds number $Re_e = U_{Bulk}2H/\eta_e$, in turn used to find the effective friction factor from (2.2). This simple approach predicts an increase in the friction factor with the particle concentration, although of different magnitude to that observed experimentally. We believe the difference is mainly due to the non-uniform particle distribution in a square duct, although inertial effects are not negligible, as will be discussed later. Modelling a turbulent flow using an effective suspension viscosity has been shown to be a good approximation for relatively small particles when the slip between fluid and particle velocity is small (Costa *et al.* 2016).

If we limit our attention to the cases with 5 % and 10 % particle volume fraction for increasing Re_{2H}, i.e. moving from figures 10(*a*) to 10(*d*), the friction factor reduces as the particle size increases. The friction even becomes marginally smaller than for single-phase flows (implying a potential drag reduction) for the LP at $Re_{2H} \approx 27\,000$ (see figure 10*d*).

If we consider the pressure drop for the highest volume fraction in this study ($\phi = 20\,\%$), conversely, the drag reduces with increasing particle size from SP to MP but increases for LP. Thus, there is a consistent non-monotonic trend at $\phi = 20\,\%$. This observation highlights the difficulties of *a priori* estimation of the pressure drop in suspension flows. For this high concentration, LP have the maximum relative pressure drop at the smallest Re_{2H}, whereas SP have the maximum relative pressure drop at the highest Re_{2H}. Interestingly, Matas *et al.* (2003) observed in a pipe flow geometry a non-monotonic trend for the critical Reynolds number (for onset of turbulence) as a function of the particle size.

3.2. *Particle distribution*

We will interpret our data, focusing on the particle dynamics, and therefore we start by reporting the particle concentration profiles. As seen in figure 11, for the lowest $Re_{2H} \approx 10\,000$, particles sediment towards the bottom of the duct. The three coloured lines in the figure correspond to three different spanwise planes: $z/H = 0$, 0.4 and 0.8. At low volume fraction, $\phi = 5\,\%$ (see figure 11*a,b*), the particle concentration is highest at the bottom wall, due to the presence of a particle-wall layer. Above this layer, the concentration reduces and goes to almost zero at the top wall. The concentration is higher on the plane of the wall bisector ($z/H = 0$) and decreases while moving towards the sidewall ($z/H = 1$). For the highest volume fraction $\phi = 20\,\%$ (cf. figure 11(*c,d*) where we change the x-scale from 0–35 % to 0–60 %), particles tend to form a much denser bed with an area concentration close to 40 % above the particle-wall layer.

On the other hand, for the highest $Re_{2H} \approx 27\,000$, particles are dispersed throughout the volume of the duct since inertial forces overcome the influence of gravity (see figure 12). Figure 12(*a,b*) shows the particle concentration at $\phi = 5\,\%$; compared to the case with $Re_{2H} \approx 10\,000$, the particle distribution is more uniform. For $\phi = 20\,\%$, the concentration distribution shows nearly equal peaks of high concentration at the top and the bottom walls along with a maximum at the centre of the duct. More detailed features about the particle distribution profile will be discussed together with the velocity field in § 3.3.

3.3. *Velocity statistics*

Next, we report and discuss the measurement of fluid and particle velocity statistics. We recall that PIV and PTV were not possible for the SP, which were not transparent

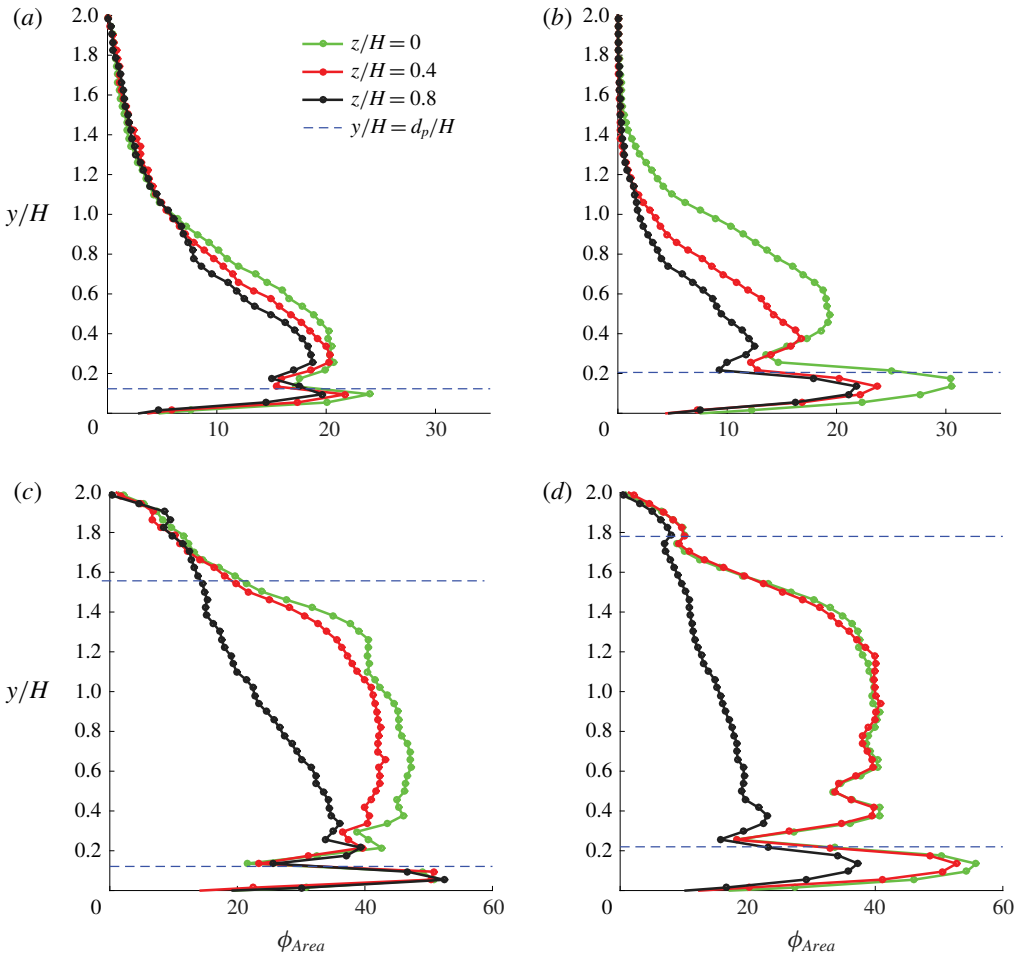

FIGURE 11. (Colour online) Area concentration profile at low $Re_{2H} \approx 10\,000$ in three spanwise planes. (*a*,*b*) Medium-sized (MP) and large-sized particles (LP) at $\phi = 5\,\%$, respectively; (*c*,*d*) MP and LP at $\phi = 20\,\%$, respectively.

enough. We therefore report velocity statistics for MP and LP and focus on the extreme cases in terms of particle volume fraction ϕ (5 and 20 %) and bulk Reynolds number Re_{2H} (10 000 and 27 000). Thus, there are four different cases for each particle size.

3.3.1. *Fully suspended particles ($Re_{2H} \approx 27\,000$)*

As the Reynolds number is increased, more particles are drawn into suspension; see figure 12. At the highest $Re_{2H} \approx 27\,000$, the values of Rouse number $Ro = 0.6$ for MP and 1.2 for LP lie in the 'suspended-load' regime (Fredsøe & Deigaard 1992). We therefore start by examining the results at high Re_{2H}, initially assuming that the effect of gravity is negligible.

High volume fraction ($\phi = 20\,\%$). Let us first focus on the case with the highest volume fraction, $\phi = 20\,\%$, where the flow statistics differ most from the corresponding single-phase case. We compare the velocity profiles for both MP and LP in three

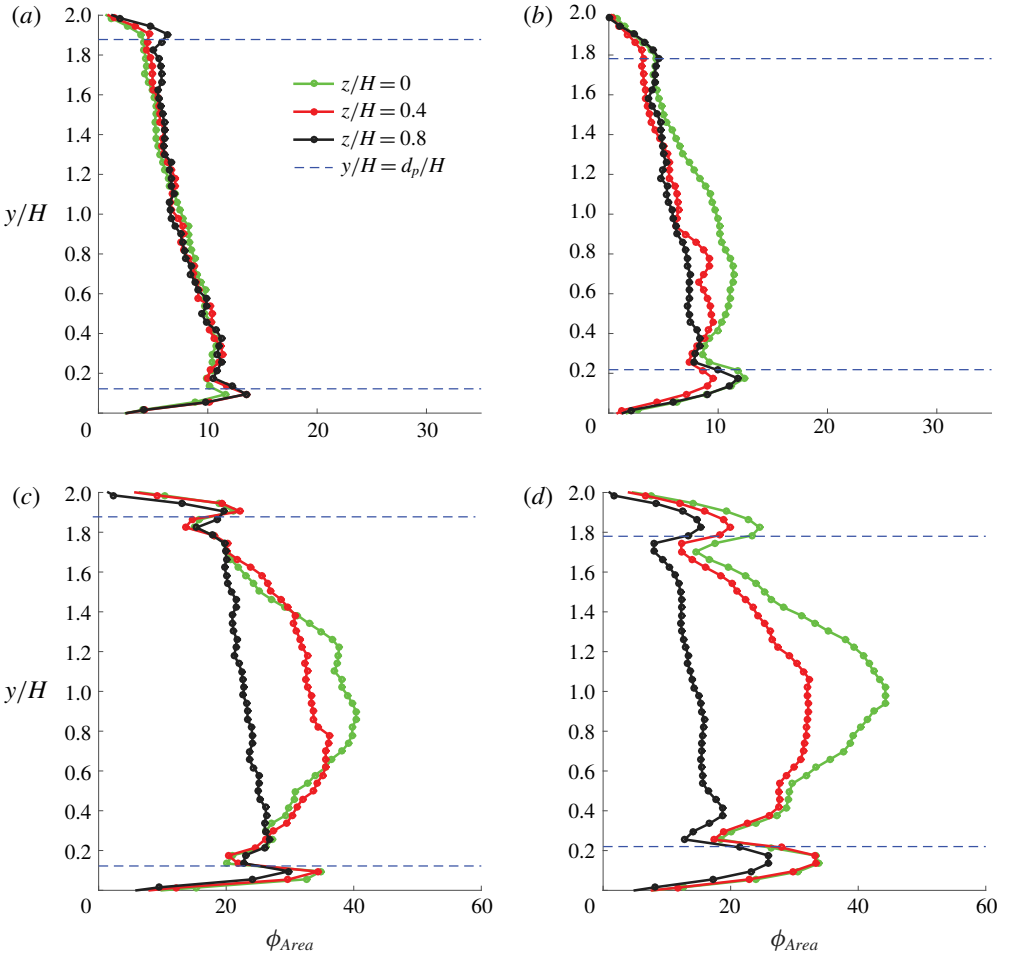

FIGURE 12. (Colour online) Area concentration profile at high $Re_{2H} \approx 27\,000$ in three spanwise planes. (*a*,*b*) Medium-sized (MP) and large-sized particles (LP) at $\phi = 5\,\%$, respectively; (*c*,*d*) MP and LP at $\phi = 20\,\%$, respectively.

different spanwise planes, $z/H = 0$, 0.4 and 0.8, in figure 13(*a–c*). In the plots, the profiles for LP have been shifted to the right for clarity and the corresponding x-axis is on the top. Velocity profiles for the single-phase case at the same bulk Re_{2H} are displayed with a green line for comparison purposes.

Figure 13(*a–c*) shows the mean-streamwise velocity profiles for both the fluid and particle phase. For MP, the velocity in the central region of the plane $z/H = 0$ (see figure 13*a*) tends to be parabolic, characteristic of laminar flow, as compared to the flatter single-phase turbulent velocity profile; we note that a laminar-like velocity profile has also been reported in Picano *et al.* (2015) from simulations of spheres in channel flow. On the other hand, the fluid velocity does not change significantly when compared to the single-phase case for LP. A similar change is also seen in the plane at $z/H = 0.4$; see figure 13(*b*). We believe this to be a particle size effect: the LP are approximately 0.1 times the full duct height ($2H/d_p = 9$). Due to their relatively larger size, they transport momentum from high-velocity regions to low-velocity regions (i.e.

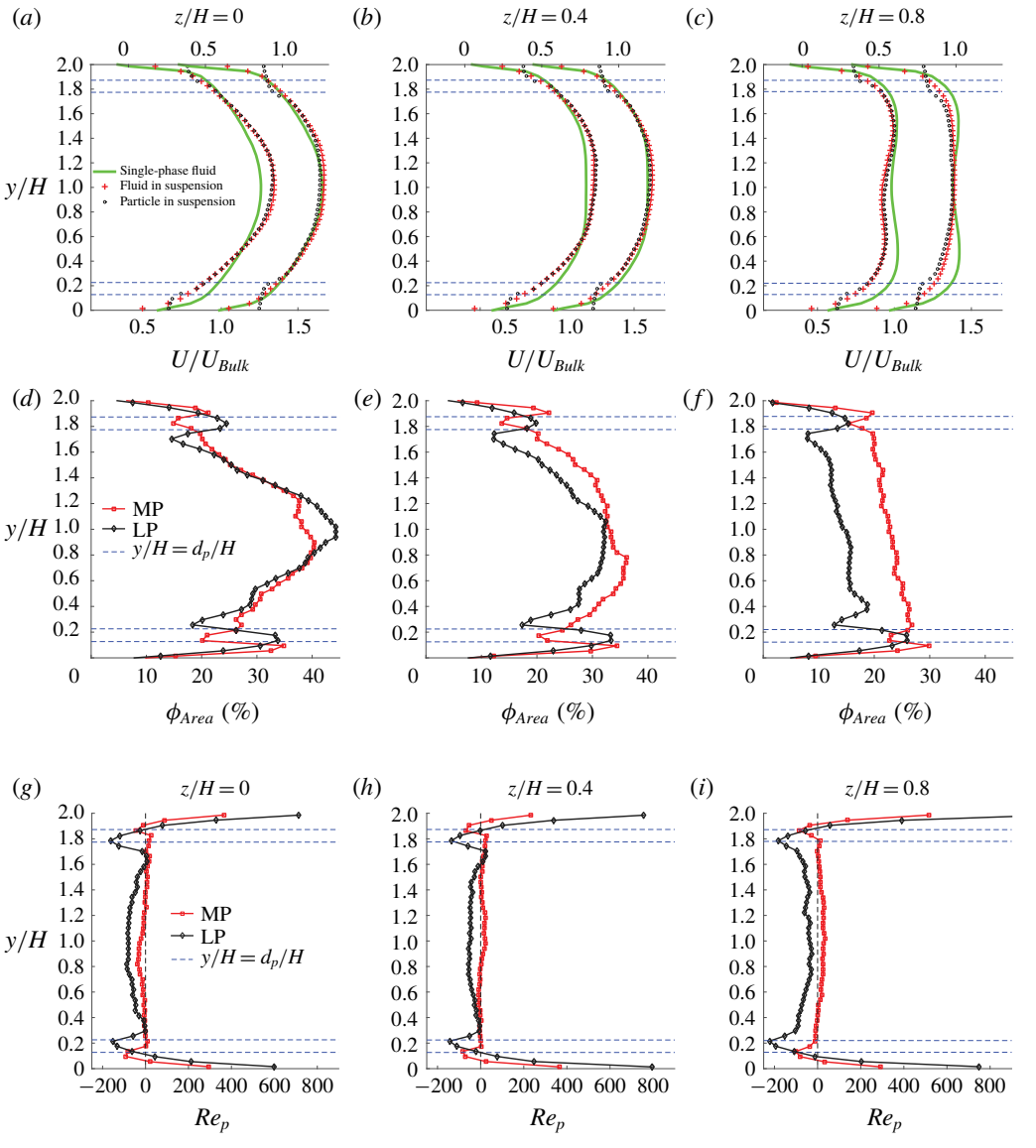

FIGURE 13. (Colour online) Medium (MP, $2H/d_p = 16$) and large-sized particles (LP, $2H/d_p = 9$) in full suspension, $Re_{2H} \approx 27\,000$, $\phi = 20\,\%$, at three spanwise planes, $z/H = 0$, 0.4 and 0.8. Shown above are profiles for the mean-streamwise velocity (*a–c*), particle area concentration (*d–f*) and particle Reynolds number Re_p (*g–i*). The blue dashed lines correspond to one particle diameter for each of the two particle sizes. The profiles in figures (*a–c*) that have been shifted to the right correspond to LP. The corresponding *x*-axis for these shifted profiles is on the top of the plots.

from the centre towards the walls) more efficiently, which leads to a relatively flatter streamwise velocity profile.

The velocity in the plane closest to the sidewall ($z/H = 0.8$ in figure 13*c*) reduces at all elevations. This is expected because an increase of the flow rate in the duct core

(close to $z/H = 0$) should be compensated by a decrease in flow rates close to the sidewalls if the volume flow rate is constant. For LP, the absence of velocity maxima of the fluid mean-streamwise velocity profile at the top and bottom suggests that the secondary flow, i.e. corner vortices that carry streamwise momentum from the centre towards the corners, has weakened. This may be explained by the reduction of the turbulence activity, responsible for the generation of this secondary flow, which will be documented later.

The particle mean-streamwise velocity for both MP and LP is almost the same as that of the fluid except close to the top and bottom walls, due to the slip of the particles at the walls (also seen in the simulations by Picano *et al.* 2015 and Costa *et al.* 2016). As mentioned above, MP and LP have diameters of the order $d_p/\delta_\nu \approx$ 90 and 165, with δ_ν the viscous length scale of the single-phase flow at the same Re_{2H}. This means that both particles extend well into the log layer of the reference single-phase flow.

To understand the modification in the mean-streamwise velocity, we display in figure 13(*d–f*) the concentration profiles for MP and LP side by side at the same spanwise position. The wall layering at the top and bottom walls is clear. Particles in the duct mid-plane tend to migrate towards the centre (see figure 13*d*). This is due to inertial shear-induced migration, as explained in Fornari *et al.* (2016*b*). The concentration is more uniform close to the sidewalls (see figure 13*f*) due to the high-intensity streaky turbulence in that region, as observed in PIV movies. These vigorous velocity fluctuations tend to keep the particles in uniform suspension. However, the concentration of the LP at $z/H = 0.8$ is lower than that of the MP because this plane nearly corresponds to the particle depleted layer, one diameter away from the sidewall. Note again that the concentration profiles appear a little skewed towards the bottom half due to sedimentation.

The difference between the particle velocity U_p and the fluid velocity U_f, i.e. the apparent particle slip velocity, is depicted in figure 13(*g–i*) in terms of the particle Reynolds number $Re_p = (U_p - U_f)d_p/\nu_f$. As mentioned before, the slip velocity has its maximum value at the wall ($Re_p \approx 500$). This quantity is most likely overestimated near the wall, as the apparent particle motion is assumed to be only translational as measured using the PTV technique. In the near-wall region, particles are more likely to rotate according to the local fluid vorticity so that the local velocity of the solid phase is closer to the fluid phase, yielding lower particle Reynolds number. The estimate of Re_p becomes more accurate towards the core as the particle mean angular velocity becomes small. Close to the centre of the duct, the MP appear to travel with the mean fluid velocity, resulting in a low Re_p. However, in the same region, the LP are slower than the fluid, with Re_p of the order of 50. This could be due to the relatively higher relaxation time of the LP (see Stokes number in figure 8*c*) and to the higher concentration in the duct core.

A finite-particle Reynolds number Re_p leads, in laminar flows, to inertial shear thickening, as described in Picano *et al.* (2013): finite inertia at the particle scale affects the particle relative motions and effectively increases the excluded volume around each particle. This increase in the effective excluded volume results in an enhanced effective viscosity. For a fully turbulent flow, it is worthwhile considering the theory of Costa *et al.* (2016), who showed that a layer of particles, flowing near the wall with significant apparent slip velocity, is responsible for an increase in drag which cannot be modelled by an effective suspension viscosity. This theory assumes that the flow domain can be split into two regions: (i) a region close to the wall, where the difference between the mean velocity of the two phases is substantial, and

(ii) a region away from the wall, where the mean flow is well represented by the continuum limit of a Newtonian fluid with an effective viscosity. This has been shown to predict the mean velocity and drag of turbulent plane channel flow. However, the particles studied here are larger than those in Costa *et al.* (2016); also a square duct has two inhomogeneous directions and the two additional walls on the sides prevent the particle lateral motion. This confinement leads to a peak in the particle concentration profile at the duct core at high ϕ, as shown in Fornari *et al.* (2018*a*). The presence of weak secondary flow in the square duct would also influence the momentum balance, thus causing further deviations from a channel flow, where no secondary motion is seen.

The root mean square (r.m.s.) of the fluid velocity fluctuations for both MP and LP is displayed in figure 14. As in the previous figure, the statistics for LP are shifted towards the right for clarity. The fluctuations in the streamwise direction reduce, marginally for MP and more substantially for LP, in all three planes considered (see figure 14*a–c*). This reduction is higher on the bottom half of the duct due to the asymmetry in the concentration distribution caused by gravity. The wall-normal velocity fluctuations (see figure 14*d–f*) reduce by nearly the same amount for both MP and LP in all three spanwise planes examined. The reduction is highest close to the centre, which could be related to the peak in particle concentration in this region. The measured fluid Reynolds stress component (figure 14*g–i*) reduces more for LP than MP as compared to the single-phase case. Thus, it appears that LP are more effective in damping the turbulent fluctuations. This relatively larger damping of turbulence in LP might be the reason for the reduction of secondary motion, and consequently the disappearance of the maxima in the mean-streamwise velocity profile near the corners in the $z/H = 0.8$ plane (cf. figure 13*c*).

Despite the larger reduction of the three measured components (out of six) of the fluid Reynolds stress, $\overline{u'u'}$, $\overline{v'v'}$ and $\overline{u'v'}$ for LP over MP, the pressure drop for LP is larger than for MP. In particular, it increases by approximately 7 % compared to the single-phase case for LP, whereas the increase is just 1 % for MP. At this highest Re_{2H}, the uncertainty in measuring the friction factor is of the order of ± 1 % (cf. figure 9). Recalling that the total momentum transfer arises from the contribution of viscous, turbulent and particle-induced stresses (Lashgari *et al.* 2014), it can be inferred that the reduction in turbulent stresses is compensated by an even higher increase in the particle-induced stress (assuming that the viscous stresses are smaller at such high Re_{2H}). As the particle-induced stress is higher for LP than MP, the overall stress is higher for LP than MP despite the reduced turbulence activity in the flow seeded with LP.

Low volume fraction ($\phi = 5\,\%$). Next we examine the velocity statistics for $\phi = 5\,\%$ and the largest Reynolds number considered, i.e. when the role of settling is assumed minor. Figure 15(*a–c*) shows the mean-streamwise velocity for both MP and LP side by side. Unlike the case with $\phi = 20\,\%$ discussed above, the overall changes with respect to the single-phase flow are marginal. This is consistent with the friction factor in figures 9 and 10(*d*), which is very close to the values for single-phase flow at this volume fraction. The mean particle velocity is also nearly the same as that of the fluid, except at the walls. The distance from the walls over which the particle velocity deviates from the fluid velocity is larger for LP due to their larger size. One can also note that the magnitude of this slip velocity is higher for LP, as the particle covers a larger distance from the wall and is exposed to a larger velocity difference.

Figure 15(*d–f*) compares the particle area concentration profiles for MP and LP at the same spanwise location and nominal concentration of 5 %. It can be seen

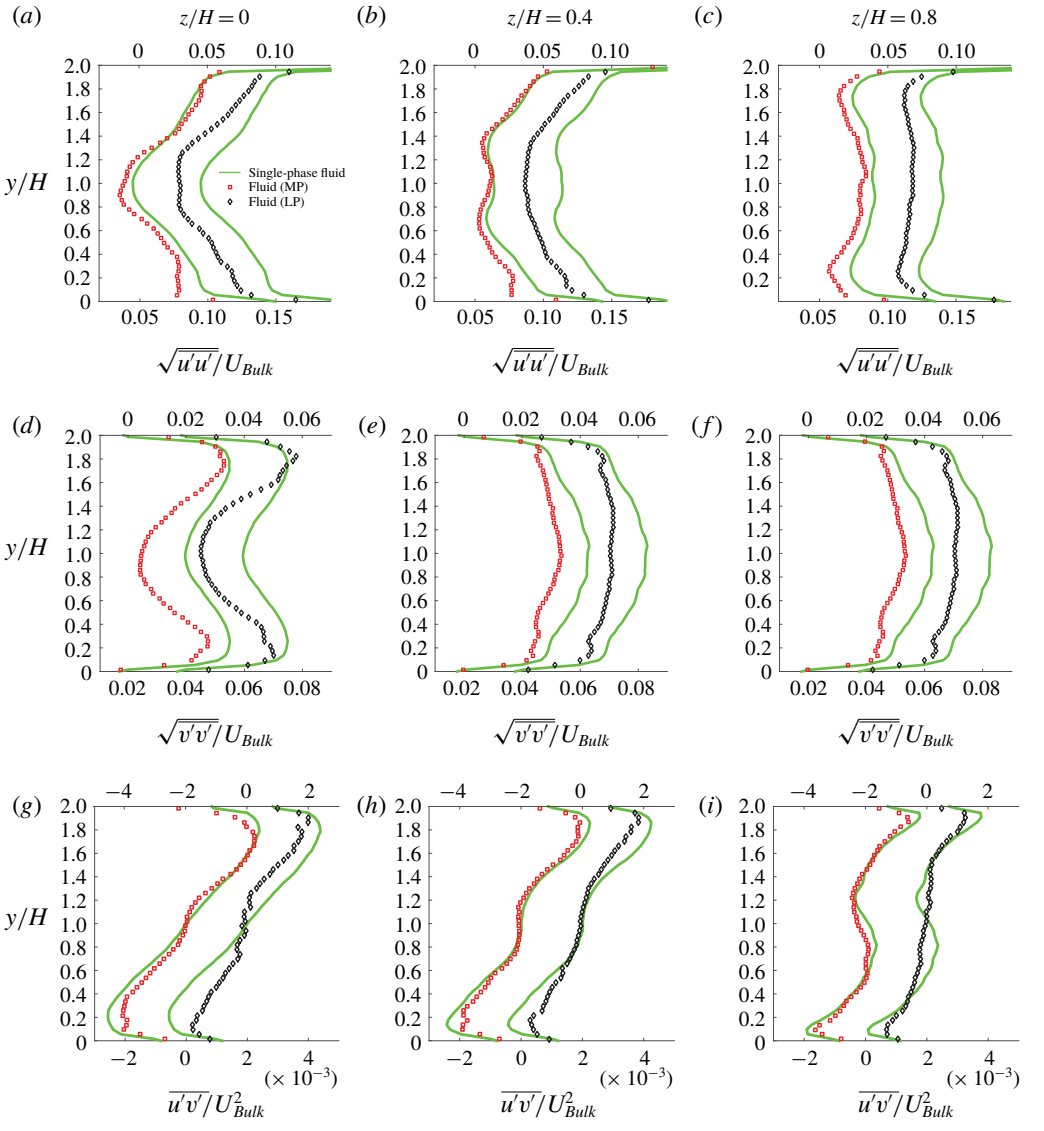

FIGURE 14. (Colour online) Medium (MP, $2H/d_p = 16$) and large-sized particles (LP, $2H/d_p = 9$) in full suspension: $Re_{2H} \approx 27\,000$, $\phi = 20\,\%$. Shown above are the profiles for the streamwise velocity fluctuations (*a–c*), wall-normal velocity fluctuations (*d–f*) and Reynolds stresses (*g–i*) of the fluid phase. Profiles shifted to the right correspond to LP and the corresponding x-axis is on the top.

that the concentration is higher at the bottom than at the top wall, indicating the presence of mild sedimentation even at these high Re_{2H}. The weak asymmetry in the concentration distribution is reflected in the mean-streamwise velocity profile. Nevertheless, the difference is marginal and one can assume that the effect of fluid inertia is much larger than the effect of gravity on the particle dynamics. The concentration profiles show a local peak in concentration at the bottom and top walls (stronger at the bottom wall), suggesting the presence of a particle-wall layer. Also,

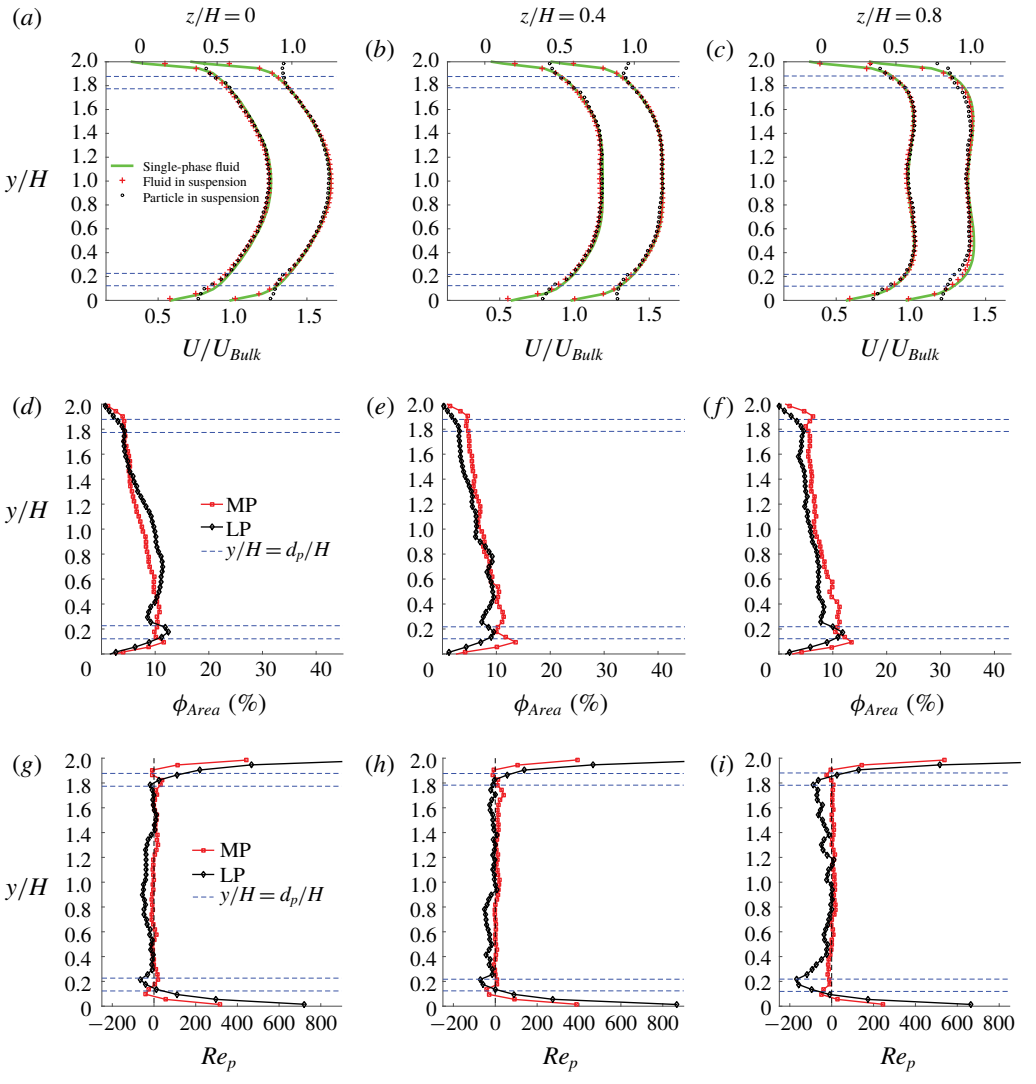

FIGURE 15. (Colour online) MP ($2H/d_p = 16$) and LP ($2H/d_p = 9$) in full suspension: $Re_{2H} \approx 27\,000$, $\phi = 5\,\%$. Shown above are profiles for the mean-streamwise velocity (*a–c*), particle area concentration (*d–f*) and particle Reynolds number Re_p (*g–i*). The blue dashed lines correspond to one particle diameter for each of the two particle sizes. Profiles in figures (*a–c*), shifted to the right correspond to LP and the corresponding x-axis is on the top.

the peak of the concentration profile close to the wall does not occur at one particle radius, but slightly beyond that. This is due to the fact that the particles in the wall layer do not simply roll in contact with the wall at all times. Instead, they roll, slide and often bounce due to turbulent fluctuations and particle collisions. In addition, the (repulsive) wall-normal lubrication force also contributes to the shifted concentration peak. In the mid-plane at $z/H = 0$, the concentration of LP has a second local maximum at $y/H \approx 0.7$: this is a signature of the increased inertial shear-induced migration.

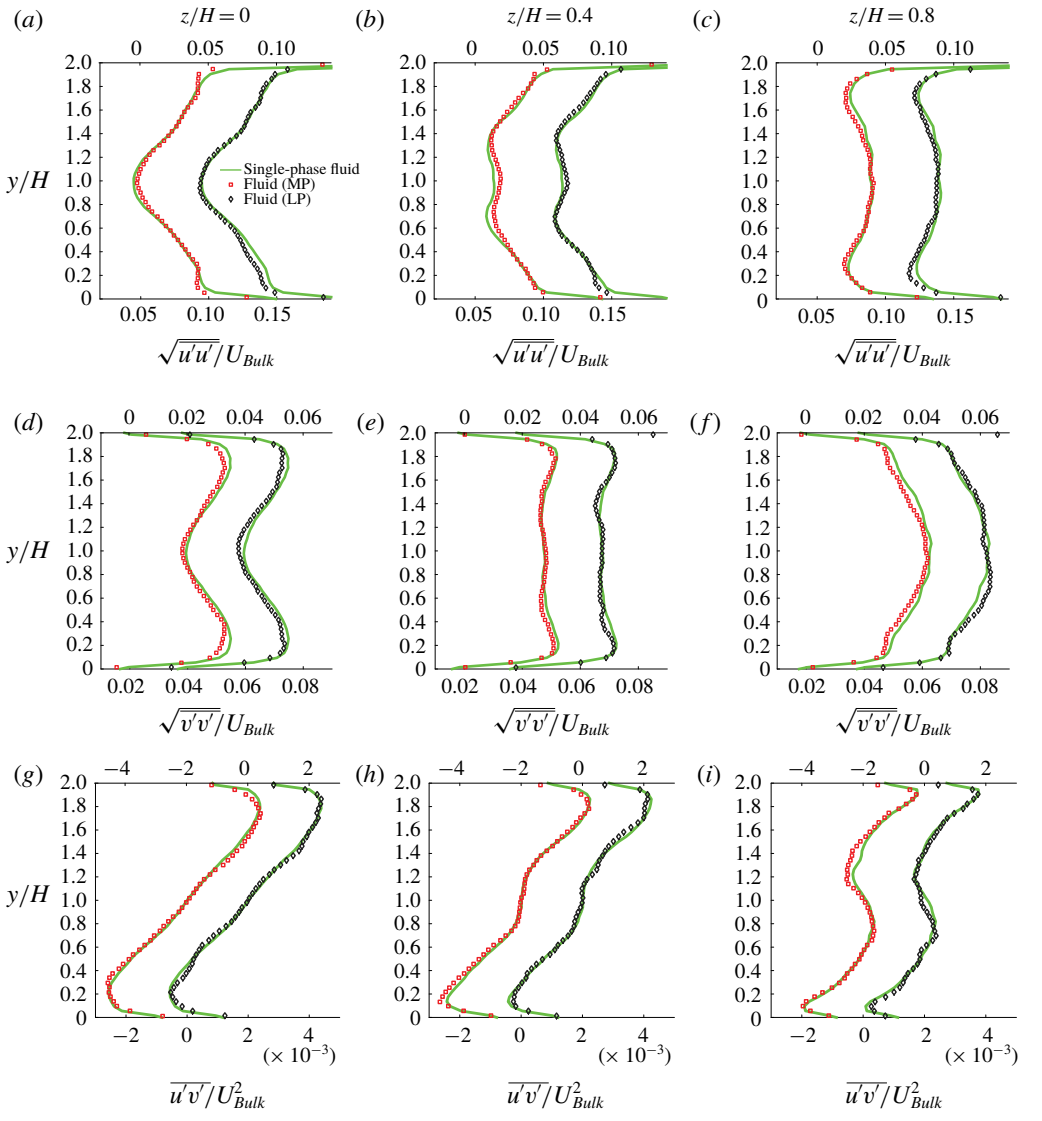

FIGURE 16. (Colour online) MP ($2H/d_p = 16$) and LP ($2H/d_p = 9$) in full suspension: $Re_{2H} \approx 27\,000$, $\phi = 5\,\%$. Shown above are the profiles for the streamwise velocity fluctuations (*a–c*), wall-normal velocity fluctuations (*d–f*) and Reynolds stresses (*g–i*) of the fluid phase. Profiles shifted to the right correspond to LP and the corresponding x-axis is on the top.

We next consider the slip velocity between the two phases. Comparing to the case at $\phi = 20\,\%$, the magnitude of the particle Reynolds number Re_p is smaller at this lower volume fractions. This effect is even more pronounced for MP, where $Re_p \approx 0$ in the core of the flow (see figure 15*g–i*). This smaller discrepancy between the velocity of the two phases is likely a consequence of a smaller frequency of particle–particle short-range interactions in more dilute conditions.

The r.m.s. of the streamwise and wall-normal velocity fluctuations in the three planes of measurement are displayed in figures 16(*a–c*) and 16(*d–f*), whereas the

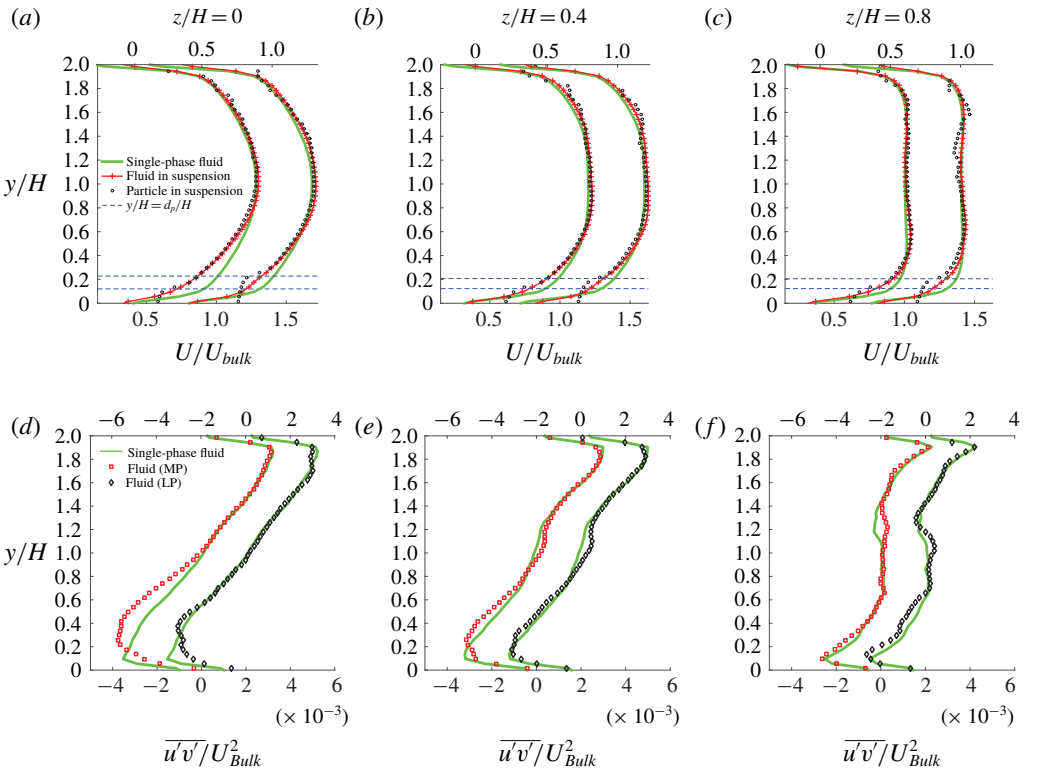

FIGURE 17. (Colour online) Comparison of mean velocity and Reynolds stress for medium (MP) and large-sized particles (LP): $Re_{2H} \approx 10\,000$, $\phi = 5\,\%$. (*a–c*) Mean-streamwise velocity and (*d–f*) Reynolds stress. The profiles in figures (*a–f*) that have been shifted to the right correspond to LP. The corresponding x-axis for these shifted profiles is on the top of the figures.

Reynolds shear stress $\overline{u'v'}$ is reported in figure 16(*g–i*). A small local attenuation of the streamwise velocity fluctuations can be observed for MP close to the bottom and top wall (see figure 16*a*), in correspondence with the particle-wall layer, but, on the whole, it appears that for $\phi = 5\,\%$ the velocity fluctuations and their correlations do not deviate significantly from the single-phase case. Thus, the presence of particles does not cause significant differences in the second-order statistics. As shown in figure 10(*d*), the pressure drop for both MP and LP is approximately 1 % lower than for the single-phase flow. We can therefore infer that the stress induced by the particles does not have a major contribution towards the total stress for $\phi = 5\,\%$ at the highest $Re_{2H} \approx 27\,000$, and turbulence is not significantly modified.

3.3.2. *Sedimenting particles ($Re_{2H} \approx 10\,000$)*

We now turn our attention to the case with the lowest $Re_{2H} \approx 10\,000$, characterized by particles in sedimentation and resuspension, as seen by the concentration distributions in figure 11. The Rouse number Ro is now 1.5 for MP and 3 for LP, and ranges from the intermediate to the 'bed-load' regime according to the classification in Fredsøe & Deigaard (1992).

Low volume fraction ($\phi = 5\,\%$). As shown in figure 11(*a,b*), the particles reside mostly in the bottom half of the duct so that the velocity statistics are modified there the most. The fluid mean-streamwise velocity, depicted in figure 17(*a–c*), decreases in the region with higher particle concentration. The pressure drop for this low concentration is similar for both particle sizes (approximately 12 % higher than the single-phase flow) and the mean flow is quite similar as well.

The Reynolds shear stress is shown in figure 17(*d–f*) for the same experiments; it deviates the most from the single-phase case in the region of high particle concentration close to the bottom wall. It is interesting to note that the MP increase the fluctuations more than the LP in the region of high particle concentration. We believe that this is a particle number effect. The MP are approximately six times more in number than the LP at the same volume fraction. At such relatively low Re_{2H}, particle-induced effects increase as particle size reduces (Lin *et al.* 2017). We also note that the peak in the Reynolds shear stress is displaced away from the bottom wall on the plane $z/H = 0$ and the streamwise fluid fluctuations are suppressed in the particle layer at the bottom wall for both MP and LP (see figure 21 in the Appendix).

High volume fraction ($\phi = 20\,\%$). The particle distribution, when increasing the volume fraction to 20 % at the same $Re_{2H} \approx 10\,000$, was discussed in connection with figures 11(*c,d*) for MP and LP. As noted above, the concentration is highest in the plane $z/H = 0$ and decreases towards the sidewalls. Particle layering is clearly visible across the height of the channel, especially for the LP, which is indicative of a moving porous bed. The concentration peak corresponding to the particle layer at the top wall measured at higher Reynolds numbers starts to appear already at this flow rate.

The fluid mean-streamwise velocity is substantially skewed (see figure 18*a–c*) with a large reduction in the lower half and an increase in the top half. The maximum streamwise velocity is higher for the case with MP, which can be explained by the reduced porosity of the moving bed for MP. As MP are smaller, they are more closely packed, which lowers the bed porosity and causes a decrease of the fluid velocity in all three spanwise planes. To compensate for the reduced fluid flow through the bed, the fluid accelerates in the region above the bed where the particle concentration is relatively low.

The apparent slip velocity, i.e. the difference between fluid and particle velocity, is higher for LP than MP. The 'bumpy' fluid velocity in the particle layer at the bottom wall can also be seen in all three planes, suggesting that there is a stable particle layer slowing down the flow. This also confirms that our measurement procedures can indeed reveal flow fields under such high local concentrations ($\phi \approx 50\,\%$).

The Reynolds shear stress profiles are displayed in figure 18(*d–f*). The reduced correlation of the streamwise and wall-normal component of the fluid velocity in regions of high particle concentration is clearly visible. Towards the top wall, where the particle concentration is lower, the Reynolds stresses tend to retain values similar to the single-phase case. Nevertheless, we note a small increase for the MP and a small decrease for the LP. Similar trends are observed in the intensity of the streamwise and wall-normal velocity fluctuations close to the top wall (shown in figure 22 in the Appendix). This can be understood by recalling that the maximum streamwise velocity is higher for MP than in LP. Broadly speaking, the duct can be split into two regions: a region similar to a porous medium near the bottom wall and a region similar to a duct flow with low particle concentration near the top. The Reynolds number pertaining to this upper region is higher for MP than LP owing to the higher fluid velocity. Thus, the turbulence intensities are also higher for MP.

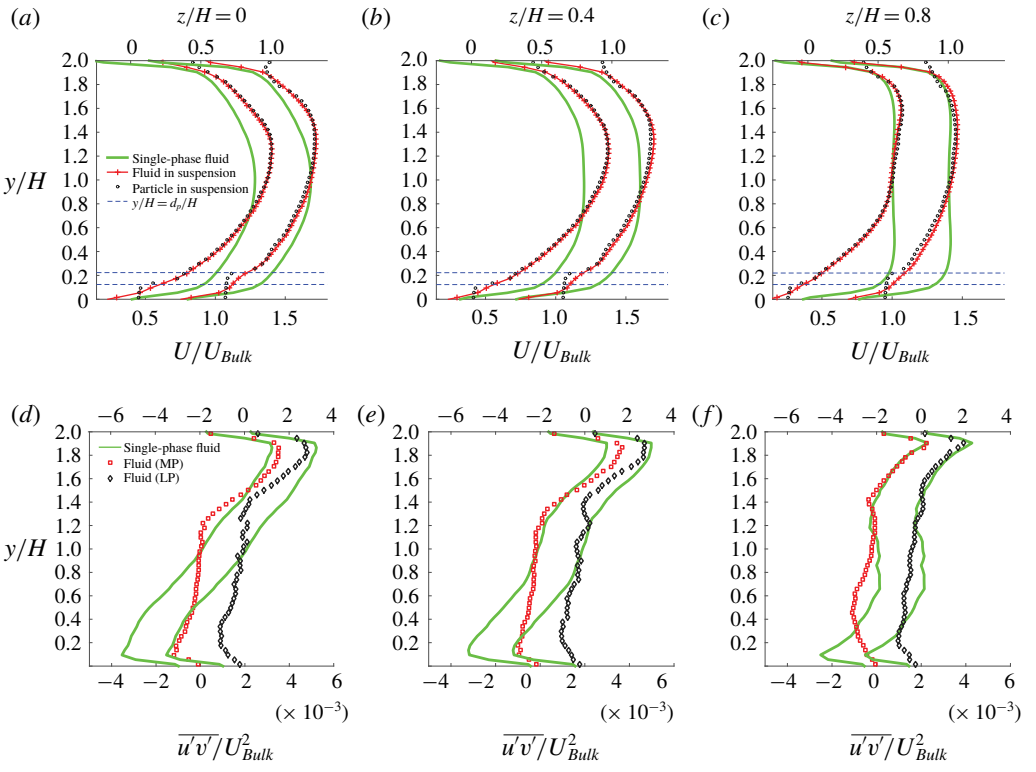

FIGURE 18. (Colour online) Comparison of mean velocity and Reynolds stress for medium (MP) and large-sized particles (LP): $Re_{2H} \approx 10\,000$, $\phi = 20\,\%$. (*a–c*) Mean-streamwise velocity and (*d–f*) Reynolds stress. Profiles shifted to the right correspond to LP and the corresponding x-axis is on the top.

Finally, we have shown in figure 10(*a*) that the pressure drop is higher with LP (approximately 50 % higher than the single-phase flow) than MP (approximately 32 % higher than the single-phase flow). LP are larger than MP and therefore form a bed of higher porosity, where the fluid flows through the gaps more effectively. Thus, these larger particles tend to be suspended more easily, despite their larger size.

4. Discussion and conclusion

We have presented measurements of pressure drop and fluid and particle velocity in a square duct laden with spherical particles for three particle volume fractions ($\phi = 5$, 10 and 20 %) and three particle sizes ($2H/d_p \approx 40$, 16 and 9). Refractive index matched (RIM) hydrogel particles in water have enabled us to use PIV and PTV techniques to measure the fluid and particle velocities up to the relatively high volume fraction of $\phi = 20\,\%$ for the two largest sizes considered. The particle-to-fluid density ratio ranges from 1.0035 to 1.01, so that, especially at the lower Reynolds number considered, settling is not negligible. In the analysis, we therefore consider the case at high Re_{2H} as a fully suspended regime, whereas at low Re_{2H} we have a low-porosity moving particle bed.

The friction factor of the suspensions is found to be significantly larger than that of single-phase duct flow at the lower Re_{2H} investigated; however, the difference

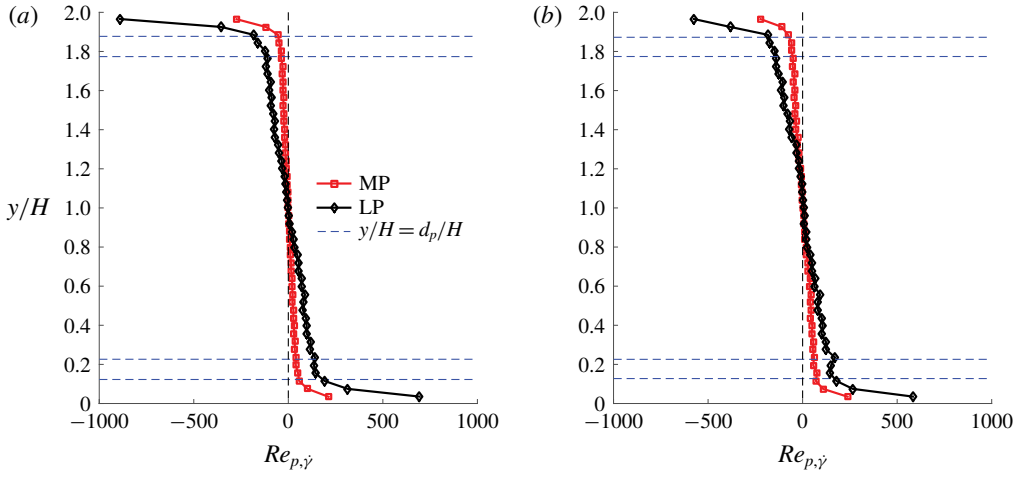

FIGURE 19. (Colour online) Shear-rate-based particle Reynolds number $Re_{p,\dot{\gamma}}$ for (*a*) $\phi = 5\,\%$ and (*b*) $\phi = 20\,\%$ at $Re_{2H} \approx 27\,000$ and $z/H = 0$.

decreases when increasing the flow rate and the total drag becomes close to, in some cases slightly lower than, in single-phase flow at the higher Reynolds number considered, $Re_{2H} = 27\,000$. With regard to the dependence on the particle size, the pressure drop is found to decrease with the particle diameter for volume fractions lower than $\phi = 10\,\%$ for nearly all Re_{2H} investigated in this study. However, at the highest volume fraction $\phi = 20\,\%$, we report a peculiar non-monotonic behaviour: the pressure drop first decreases and then increases with increasing particle size.

The decrease of the turbulent drag with particle size at the lowest volume fractions is related to an attenuation of the turbulence. The larger particles more effectively break coherent eddies in the flow and reduce the turbulent stresses. The drag increase from MP to LP at $\phi = 20\,\%$, however, occurs despite a larger reduction of the turbulent stresses and is due to significant particle-induced stresses. Indeed, focusing on the highest Re_{2H}, when gravitational effects can be neglected, the pressure drop at a given volume fraction is defined by the balance between turbulent stresses and particle-induced stresses, assuming viscous effects to be small and localized near the walls. As compared to MP, LP give a larger reduction in turbulent stresses. On the other hand, the particle-induced stresses appear to be larger for LP. This can be ascertained from the particle Reynolds number $Re_{p,\dot{\gamma}} = \dot{\gamma}(d_p/2)^2/\nu_f$, based on the local fluid shear rate $\dot{\gamma}$ and the particle radius as shown in figure 19. At the highest Re_{2H}, the $Re_{p,\dot{\gamma}}$ is larger for LP as compared to MP for all ϕ. As shown in Picano *et al.* (2013), even at $Re_{p,\dot{\gamma}} = 10$, significant inertial shear thickening is observed, especially for larger ϕ. In the present case, we observe much higher values of $Re_{p,\dot{\gamma}}$ in the near-wall region. This increase in particle-induced stress exceeds the reduction in turbulent stresses at higher ϕ and leads to the overall increase of the pressure drop for LP as compared to MP at $\phi = 20\,\%$.

To explain the cause for the non-monotonic pressure drop at the highest volume fraction $\phi = 20\,\%$ and higher Re_{2H} (where the influence of gravity on pressure drop is negligible) we consider the variation of concentration and mean-streamwise velocity profile in the plane of the wall bisector, as sketched in figure 20. Velocity and concentration measurements have been performed for LP and MP only, whereas a

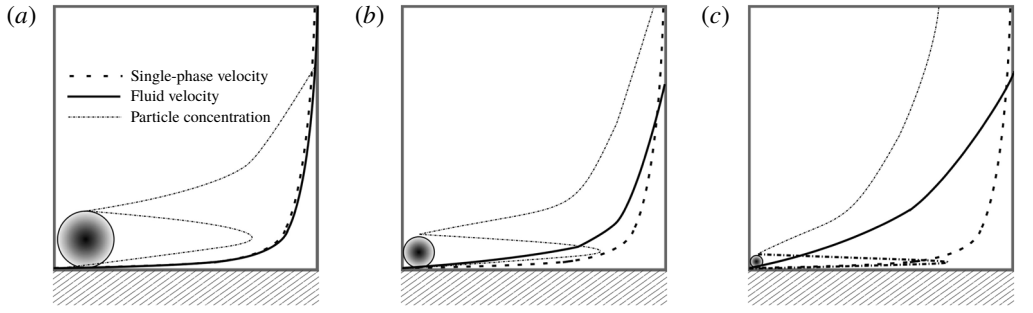

FIGURE 20. Schematic of change in mean-streamwise velocity and concentration profile in the plane of the wall bisector $z/H = 0$ for (*a*) LP, (*b*) MP and (*c*) SP at $Re_{2H} \approx 27\,000$ and $\phi = 20\,\%$.

qualitative picture is proposed for SP based on the pressure drop measurements and the simulations in Fornari *et al.* (2018*a*) for neutrally buoyant particles as their size in inner units ($20\delta_v$) is in range of our experiments for SP (15–$37\delta_v$). The simulations are, however, performed at a lower $Re_{2H} = 5600$ and the particle size in bulk units is $2H/d_p = 18$, similar to MP in experiments. The simulations confirm the largest concentration at the core of the duct at $\phi = 20\,\%$ and that the Reynolds stresses are typically lower than those of the single-phase flow, as also generally found in this study. Fornari *et al.* (2018*a*) suggest that turbulence is largely attenuated at this ϕ: turbulence production is reduced, but this is compensated by a large increase in energy injection due to particle-induced stresses.

In light of our observations, and as depicted in figure 20, the fluid velocity is very similar to the single-phase case in the case of LP, despite the larger turbulence attenuation, whereas it becomes more laminar-like for MP and is believed to be even more so as the particle size reduces to SP. The mean near-wall gradient increases as the particle size increases due to the particle layer forming at the wall and to the associated increase of the momentum transport (Costa *et al.* 2016). At a constant volume fraction the number of particles increases as the particle size decreases. The increased number of particles means more contact points and collisions between the wall and the particles, potentially increasing friction even if the momentum of each particle decreases. If so, we have two competing mechanisms as particle size reduces. This may explain the minimum in the pressure drop at MP and larger values for SP and LP. Note that SP are yet significantly larger than the small scales in the flow, of the order of about 30 viscous units, and that the total drag is in any case above that of single-phase turbulence at $\phi = 20\,\%$ but below that of a turbulent flow with the effective suspension viscosity at the highest Reynolds number considered.

At low $\phi = 5\,\%$–$10\,\%$, Fornari *et al.* (2018*a*) found that the turbulence production is slightly larger than in single-phase flow. Together with energy injection due to the presence of particles, the overall turbulence activity is found to increase by a few per cent. In our experiments, at $\phi = 5\,\%$ and high Re_{2H}, the mean-streamwise velocity and the fluid Reynolds stress profiles do not change substantially as compared to single-phase flow between MP and LP. Nevertheless, a decreasing drag from SP to LP suggests that any increase in turbulence activity is a decreasing function of the particle size. As mentioned above, as larger particles have more inertia, they do not follow the fluid as nicely as smaller particles do, and display greater resistance to deformation. Additional experimental investigations close to the wall and at $\phi = 10\,\%$,

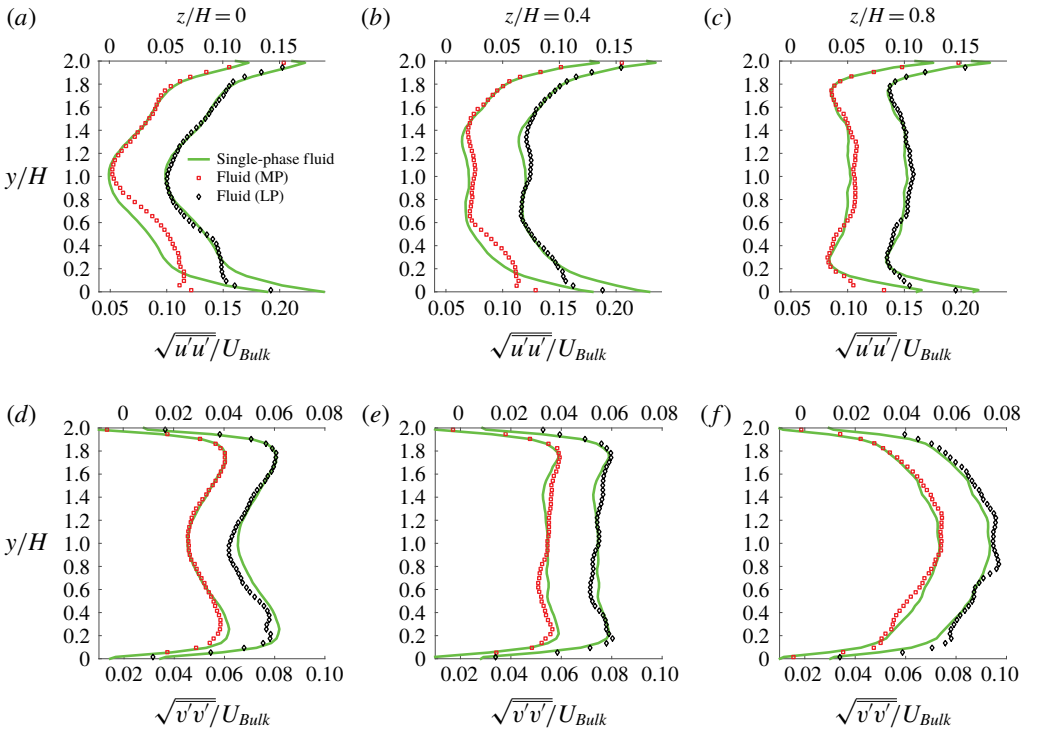

FIGURE 21. (Colour online) Comparison of streamwise (*a–c*) and wall-normal (*d–f*) r.m.s. velocities for medium (MP) and large-sized particles (LP): $Re_{2H} \approx 10\,000$, $\phi = 5\,\%$. Profiles shifted to the right correspond to LP and the corresponding x-axis is on the top.

along with detailed numerical simulations for particles with sizes corresponding to SP and LP, are needed to shed light on this.

At lower Re_{2H} (e.g. 10 000 and 15 000) settling effects become important, especially at $\phi = 20\,\%$, when particles move as part of a relatively dense particle bed and particles close to the bottom wall are shielded from the fast-moving fluid above them. At lower ϕ the thickness of the sediment bed is smaller, and hence a larger fraction of particles can be resuspended by the moving fluid. In our experiments at constant flow rate, we observe the fluid flow above the MP bed to be faster, as these smaller particles form a bed of lower permeability, and the drag to be large for LP, as these contribute to the momentum transfer with larger particle-induced stresses. As discussed above, the density of SP is higher than MP and LP (see table 1) and their Shields number lies in between the values for MP and LP. This can explain why we have an intermediate value of pressure drop for SP at these two lower Re_{2H} and $\phi = 20\,\%$. As Re_{2H} increases, more particles are suspended in the bulk of the flow, and the total drag can be explained by the inertial effects and particle dynamics just discussed.

It is also noteworthy that the total drag is above that of a continuum medium with an effective suspension viscosity at $Re_{2H} \approx 10\,000$ and is below that value when increasing the particle size and the flow Reynolds number, which may be explained by turbulence modulations and particle migrations inside the duct. This confirms

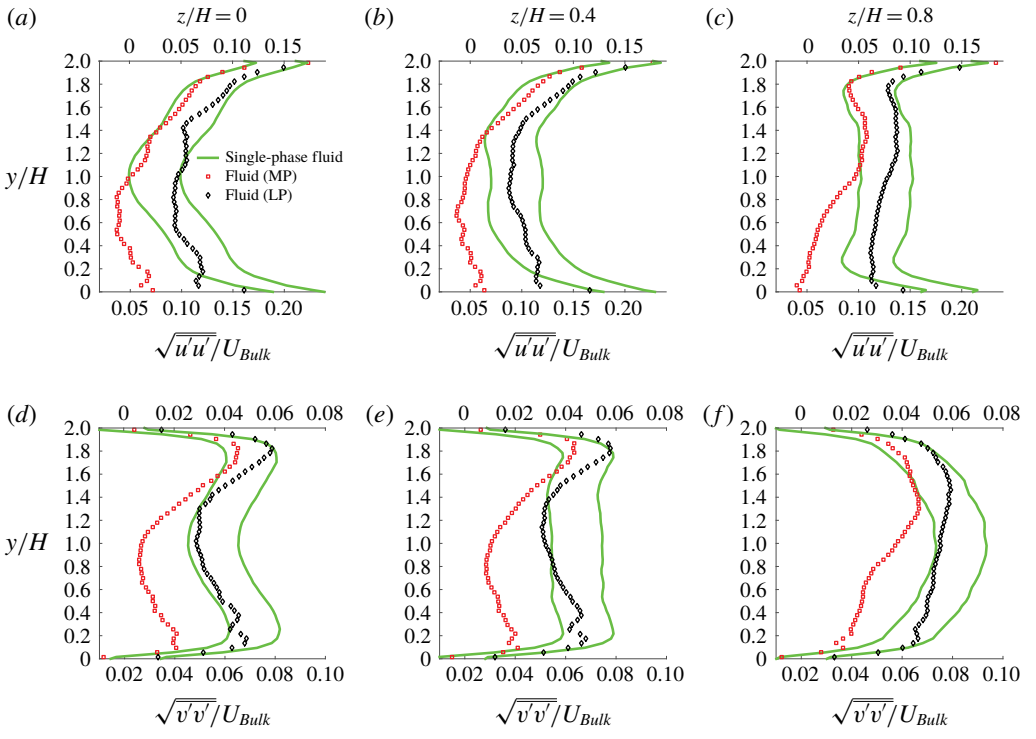

FIGURE 22. (Colour online) Comparison of streamwise (*a–c*) and wall-normal (*d–f*) r.m.s. velocities for medium (MP) and large-sized particles (LP): $Re_{2H} \approx 10\,000$, $\phi = 20\,\%$. Profiles shifted to the right correspond to LP and the corresponding x-axis is on the top.

that particle dynamics and inhomogeneities are fundamental for accurate models of suspension flows in the turbulent regime, as shown for their rheological behaviour in simple laminar shear flows.

Acknowledgements

This work was supported by the European Research Council grant no. ERC-2013-CoG-616186, TRITOS, from the Swedish Research Council (VR), through the Outstanding Young Researcher Award to L.B.

Appendix

For completeness, we report in figure 21 the r.m.s. of the streamwise and wall-normal velocity fluctuations for MP and LP at $Re_{2H} \approx 10\,000$ and $\phi = 5\,\%$. The figure shows that the streamwise velocity fluctuations increase in the case of MP in the lower part of the duct. Very close to the bottom wall, the streamwise velocity fluctuations reduce both for MP and LP. Similarly, figure 22 displays the r.m.s. of the streamwise and wall-normal velocity fluctuations for MP and LP at $Re_{2H} \approx 10\,000$ and $\phi = 20\,\%$.

REFERENCES

ABBAS, M., MAGAUD, P., GAO, Y. & GEOFFROY, S. 2014 Migration of finite sized particles in a laminar square channel flow from low to high Reynolds numbers. *Phys. Fluids* **26** (12), 123301.

ABBAS, M., POUPLIN, A., MASBERNAT, O., LINÉ, A. & DÉCARRE, S. 2017 Pipe flow of a dense emulsion: homogeneous shear-thinning or shear-induced migration? *AIChE J.* **63** (11), 5182–5195.

ARDEKANI, M. N., COSTA, P., BREUGEM, W.-P., PICANO, F. & BRANDT, L. 2017 Drag reduction in turbulent channel flow laden with finite-size oblate spheroids. *J. Fluid Mech.* **816**, 43–70.

BAGNOLD, R. A. 1954 Experiments on a gravity-free dispersion of large solid spheres in a Newtonian fluid under shear. *Proc. R. Soc. Lond.* A **225**, 49–63.

BATCHELOR, G. K. 1970 The stress system in a suspension of force-free particles. *J. Fluid Mech.* **41** (3), 545–570.

BELLANI, G., BYRON, M. L., COLLIGNON, A. G., MEYER, C. R. & VARIANO, E. A. 2012 Shape effects on turbulent modulation by large nearly neutrally buoyant particles. *J. Fluid Mech.* **712**, 41–60.

BLANC, F., LEMAIRE, E., MEUNIER, A. & PETERS, F. 2013 Microstructure in sheared non-Brownian concentrated suspensions. *J. Rheol.* **57** (1), 273–292.

BRUNDRETT, E. & BAINES, W. D. 1964 The production and diffusion of vorticity in duct flow. *J. Fluid Mech.* **19** (3), 375–394.

BYRON, M. L. & VARIANO, E. A. 2013 Refractive-index-matched hydrogel materials for measuring flow–structure interactions. *Exp. Fluids* **54** (2), 1456.

CHOI, Y.-S., SEO, K.-W. & LEE, S.-J. 2011 Lateral and cross-lateral focusing of spherical particles in a square microchannel. *Lab on a Chip* **11** (3), 460–465.

CHUN, B. & LADD, A. J. C. 2006 Inertial migration of neutrally buoyant particles in a square duct: an investigation of multiple equilibrium positions. *Phys. Fluids* **18** (3), 031704.

COSTA, P., PICANO, F., BRANDT, L. & BREUGEM, W.-P. 2016 Universal scaling laws for dense particle suspensions in turbulent wall-bounded flows. *Phys. Rev. Lett.* **117** (13), 134501.

COSTA, P., PICANO, F., BRANDT, L. & BREUGEM, W.-P. 2018 Effects of the finite particle size in turbulent wall-bounded flows of dense suspensions. *J. Fluid Mech.* **843**, 450–478.

CROWE, C. T., SCHWARZKOPF, J. D., SOMMERFELD, M. & TSUJI, Y. 2011 *Multiphase Flows with Droplets and Particles*. CRC Press.

CUCCIA, N. L. 2017 The tribological properties of polyacrylamide hydrogel particles. Honours thesis, Emory University. http://pid.emory.edu/ark:/25593/rzwwz.

DEMUREN, A. O. 1991 Calculation of turbulence-driven secondary motion in ducts with arbitrary cross section. *AIAA J.* **29** (4), 531–537.

DORON, P., GRANICA, D. & BARNEA, D. 1987 Slurry flow in horizontal pipes: experimental and modeling. *Intl J. Multiphase Flow* **13** (4), 535–547.

DRAAD, A. A., KUIKEN, G. D. C. & NIEUWSTADT, F. T. M. 1998 Laminar–turbulent transition in pipe flow for Newtonian and non-Newtonian fluids. *J. Fluid Mech.* **377**, 267–312.

DUAN, Z., YOVANOVICH, M. M. & MUZYCHKA, Y. S. 2012 Pressure drop for fully developed turbulent flow in circular and noncircular ducts. *Trans. ASME J. Fluids Engng* **134** (6), 061201.

EATON, J. K. & FESSLER, J. R. 1994 Preferential concentration of particles by turbulence. *Intl J. Multiphase Flow* **20**, 169–209.

EINSTEIN, A. 1906 Eine neue Bestimmung der Moleküldimensionen. *Ann. Phys.* **324** (2), 289–306.

EINSTEIN, A. 1911 Berichtigung zu meiner Arbeit. I. Eine neue Bestimmung der Moleküldimensionen. *Ann. Phys.* **339** (3), 591–592.

ELGHOBASHI, S. & TRUESDELL, G. C. 1993 On the two-way interaction between homogeneous turbulence and dispersed solid particles. Part I. Turbulence modification. *Phys. Fluids* A **5** (7), 1790–1801.

FORNARI, W., BRANDT, L., CHAUDHURI, P., LOPEZ, C. U., MITRA, D. & PICANO, F. 2016*a* Rheology of confined non-Brownian suspensions. *Phys. Rev. Lett.* **116** (1), 018301.

FORNARI, W., FORMENTI, A., PICANO, F. & BRANDT, L. 2016*b* The effect of particle density in turbulent channel flow laden with finite size particles in semi-dilute conditions. *Phys. Fluids* **28** (3), 033301.

FORNARI, W., KAZEROONI, H. T., HUSSONG, J. & BRANDT, L. 2018*a* Suspensions of finite-size neutrally buoyant spheres in turbulent duct flow. *J. Fluid Mech.* **851**, 148–186.

FORNARI, W., PICANO, F. & BRANDT, L. 2018*b* The effect of polydispersity in a turbulent channel flow laden with finite-size particles. *Eur. J. Mech. (*B*/Fluids)* **67**, 54–64.

FRANK, M., ANDERSON, D., WEEKS, E. R. & MORRIS, J. F. 2003 Particle migration in pressure-driven flow of a Brownian suspension. *J. Fluid Mech.* **493**, 363–378.

FREDSØE, J. & DEIGAARD, R. 1992 *Mechanics of Coastal Sediment Transport*. World Scientific.

GAVRILAKIS, S. 1992 Numerical simulation of low-Reynolds-number turbulent flow through a straight square duct. *J. Fluid Mech.* **244**, 101–129.

GESSNER, F. B. 1973 The origin of secondary flow in turbulent flow along a corner. *J. Fluid Mech.* **58** (1), 1–25.

GONG, J., HIGA, M., IWASAKI, Y., KATSUYAMA, Y. & OSADA, Y. 1997 Friction of gels. *J. Phys. Chem.* B **101** (28), 5487–5489.

GUAZZELLI, E. & MORRIS, J. F. 2011 *A Physical Introduction to Suspension Dynamics*. Cambridge University Press.

GURUNG, A. & POELMA, C. 2016 Measurement of turbulence statistics in single-phase and two-phase flows using ultrasound imaging velocimetry. *Exp. Fluids* **57** (11), 171.

HAMPTON, R. E., MAMMOLI, A. A., GRAHAM, A. L., TETLOW, N. & ALTOBELLI, S. A. 1997 Migration of particles undergoing pressure-driven flow in a circular conduit. *J. Rheol.* **41** (3), 621–640.

HAN, M., KIM, C., KIM, M. & LEE, S. 1999 Particle migration in tube flow of suspensions. *J. Rheol.* **43** (5), 1157–1174.

HO, B. P. & LEAL, L. G. 1974 Inertial migration of rigid spheres in two-dimensional unidirectional flows. *J. Fluid Mech.* **65** (2), 365–400.

HUSER, A. & BIRINGEN, S. 1993 Direct numerical simulation of turbulent flow in a square duct. *J. Fluid Mech.* **257**, 65–95.

KAUSHAL, D. R. & TOMITA, Y. 2002 Solids concentration profiles and pressure drop in pipeline flow of multisized particulate slurries. *Intl J. Multiphase Flow* **28** (10), 1697–1717.

KAWATA, T. & OBI, S. 2014 Velocity–pressure correlation measurement based on planar PIV and miniature static pressure probes. *Exp. Fluids* **55** (7), 1776.

KAZEROONI, H. T., FORNARI, W., HUSSONG, J. & BRANDT, L. 2017 Inertial migration in dilute and semidilute suspensions of rigid particles in laminar square duct flow. *Phys. Rev. Fluids* **2**, 084301.

KLEIN, S., GIBERT, M., BÉRUT, A. & BODENSCHATZ, E. 2012 Simultaneous 3D measurement of the translation and rotation of finite-size particles and the flow field in a fully developed turbulent water flow. *Meas. Sci. Technol.* **24** (2), 024006.

KOH, C. J., HOOKHAM, P. & LEAL, L. G. 1994 An experimental investigation of concentrated suspension flows in a rectangular channel. *J. Fluid Mech.* **266**, 1–32.

KULICK, J. D., FESSLER, J. R. & EATON, J. K. 1994 Particle response and turbulence modification in fully developed channel flow. *J. Fluid Mech.* **277**, 109–134.

KULKARNI, P. M. & MORRIS, J. F. 2008 Suspension properties at finite Reynolds number from simulated shear flow. *Phys. Fluids* **20** (4), 040602.

LASHGARI, I., PICANO, F., BREUGEM, W.-P. & BRANDT, L. 2014 Laminar, turbulent, and inertial shear-thickening regimes in channel flow of neutrally buoyant particle suspensions. *Phys. Rev. Lett.* **113** (25), 254502.

LASHGARI, I., PICANO, F., BREUGEM, W. P. & BRANDT, L. 2016 Channel flow of rigid sphere suspensions: particle dynamics in the inertial regime. *Intl J. Multiphase Flow* **78**, 12–24.

LIN, Z., YU, Z., SHAO, X. & WANG, L.-P. 2017 Effects of finite-size neutrally buoyant particles on the turbulent flows in a square duct. *Phys. Fluids* **29** (10), 103304.

LOISEL, V., ABBAS, M., MASBERNAT, O. & CLIMENT, E. 2013 The effect of neutrally buoyant finite-size particles on channel flows in the laminar–turbulent transition regime. *Phys. Fluids* **25** (12), 123304.

LYON, M. K. & LEAL, L. G. 1998 An experimental study of the motion of concentrated suspensions in two-dimensional channel flow. Part 1. Monodisperse systems. *J. Fluid Mech.* **363**, 25–56.

MANOORKAR, S., KRISHNAN, S., SEDES, O., SHAQFEH, E. S., IACCARINO, G. & MORRIS, J. F. 2018 Suspension flow through an asymmetric T-junction. *J. Fluid Mech.* **844**, 247–273.

MATAS, J.-P., GLEZER, V., GUAZZELLI, É. & MORRIS, J. F. 2004*a* Trains of particles in finite-Reynolds-number pipe flow. *Phys. Fluids* **16** (11), 4192–4195.

MATAS, J.-P., MORRIS, J. F. & GUAZZELLI, É. 2003 Transition to turbulence in particulate pipe flow. *Phys. Rev. Lett.* **90** (1), 014501.

MATAS, J.-P., MORRIS, J. F. & GUAZZELLI, É. 2004*b* Inertial migration of rigid spherical particles in Poiseuille flow. *J. Fluid Mech.* **515**, 171–195.

MIURA, K., ITANO, T. & SUGIHARA-SEKI, M. 2014 Inertial migration of neutrally buoyant spheres in a pressure-driven flow through square channels. *J. Fluid Mech.* **749**, 320–330.

MORRIS, J. F. 2009 A review of microstructure in concentrated suspensions and its implications for rheology and bulk flow. *Rheol. Acta* **48** (8), 909–923.

NIKURADSE, J. 1930 Untersuchungen über turbulente Strömungen in nicht kreisförmigen Rohren. *Ing.-Arch.* **1** (3), 306–332.

NOORANI, A., VINUESA, R., BRANDT, L. & SCHLATTER, P. 2016 Aspect ratio effect on particle transport in turbulent duct flows. *Phys. Fluids* **28** (11), 115103.

PICANO, F., BREUGEM, W.-P. & BRANDT, L. 2015 Turbulent channel flow of dense suspensions of neutrally buoyant spheres. *J. Fluid Mech.* **764**, 463–487.

PICANO, F., BREUGEM, W.-P., MITRA, D. & BRANDT, L. 2013 Shear thickening in non-Brownian suspensions: an excluded volume effect. *Phys. Rev. Lett.* **111** (9), 098302.

POELMA, C., WESTERWEEL, J. & OOMS, G. 2006 Turbulence statistics from optical whole-field measurements in particle-laden turbulence. *Exp. Fluids* **40** (3), 347–363.

PRANDTL, L. 1926 Über die ausgebildete Turbulenz. In *Proceedings of the 2nd International Congress for Applied Mechanics, Zurich*. *NACA Tech. Mem.* **62**, 435 (English translation).

RAFFEL, M., WILLERT, C. E., WERELEY, S. T. & KOMPENHANS, J. 2013 *Particle Image Velocimetry: A Practical Guide*. Springer.

REEKS, M. W. 1983 The transport of discrete particles in inhomogeneous turbulence. *J. Aerosol. Sci.* **14** (6), 729–739.

ROUSE, H. 1937 Modern conceptions of the mechanics of turbulence. *Trans. Am. Soc. Civil Engng* **102**, 463–505.

SARDINA, G., SCHLATTER, P., BRANDT, L., PICANO, F. & CASCIOLA, C. M. 2012 Wall accumulation and spatial localization in particle-laden wall flows. *J. Fluid Mech.* **699**, 50–78.

SEGRÉ, G. & SILBERBERG, A. 1962 Behaviour of macroscopic rigid spheres in Poiseuille flow. Part 2. Experimental results and interpretation. *J. Fluid Mech.* **14** (1), 136–157.

SHARMA, G. & PHARES, D. J. 2006 Turbulent transport of particles in a straight square duct. *Intl J. Multiphase Flow* **32** (7), 823–837.

SHIELDS, A. 1936 *Application of Similarity Principles and Turbulence Research to Bed-Load Movement*. CalTech Library.

SOLDATI, A. & MARCHIOLI, C. 2009 Physics and modelling of turbulent particle deposition and entrainment: review of a systematic study. *Intl J. Multiphase Flow* **35** (9), 827–839.

SQUIRES, K. D. & EATON, J. K. 1990 Particle response and turbulence modification in isotropic turbulence. *Phys. Fluids* **2** (7), 1191–1203.

STICKEL, J. J. & POWELL, R. L. 2005 Fluid mechanics and rheology of dense suspensions. *Annu. Rev. Fluid Mech.* **37**, 129–149.

UHLMANN, M., PINELLI, A., KAWAHARA, G. & SEKIMOTO, A. 2007 Marginally turbulent flow in a square duct. *J. Fluid Mech.* **588**, 153–162.

WERELEY, S. & GUI, L. 2003 A correlation-based central difference image correction (CDIC) method and application in a four-roll mill flow PIV measurement. *Exp. Fluids* **34** (1), 42–51.

WIEDERSEINER, S., ANDREINI, N., EPELY-CHAUVIN, G. & ANCEY, C. 2011 Refractive-index and density matching in concentrated particle suspensions: a review. *Exp. Fluids* **50** (5), 1183–1206.

WINKLER, C. M., RANI, S. L. & VANKA, S. P. 2004 Preferential concentration of particles in a fully developed turbulent square duct flow. *Intl J. Multiphase Flow* **30** (1), 27–50.

YAO, J., FAIRWEATHER, M. & ZHAO, Y. L. 2014 Numerical simulation of particle deposition in turbulent duct flows. *Ind. Engng Chem. Res.* **53** (8), 3329–3341.

YEO, K. & MAXEY, M. R. 2013 Dynamics and rheology of concentrated, finite-Reynolds-number suspensions in a homogeneous shear flow. *Phys. Fluids* **25** (5), 053303.

YUEN, H. K., PRINCEN, J., ILLINGWORTH, J. & KITTLER, J. 1990 Comparative study of Hough transform methods for circle finding. *Image Vis. Comput.* **8** (1), 71–77.

ZARRAGA, I. E., HILL, D. A. & LEIGHTON, D. T. JR. 2000 The characterization of the total stress of concentrated suspensions of noncolloidal spheres in Newtonian fluids. *J. Rheol.* **44** (2), 185–220.

ZHAO, L. H., ANDERSSON, H. I. & GILLISSEN, J. J. J. 2010 Turbulence modulation and drag reduction by spherical particles. *Phys. Fluids* **22** (8), 081702.